

Experimental Simulation and Limitations of Quantum Walks with Trapped Ions

R Matjeschk^{1,2}, Ch Schneider^{2,3}, M Enderlein^{2,3}, T Huber^{2,3}, H Schmitz², J Glueckert² and T Schaetz^{2,3}

¹ Institut für Theoretische Physik, Leibniz Universität Hannover, Appelstr. 2, 30167 Hannover, Germany

² Max-Planck-Institut für Quantenoptik, Hans-Kopfermann-Str. 1, 85748 Garching, Germany

³ Albert-Ludwigs-Universität Freiburg, Physikalisches Institut, Hermann-Herder-Str. 3, 79104 Freiburg, Germany

E-mail: robert.matjeschk@itp.uni-hannover.de

Abstract. We examine the prospects of discrete quantum walks (QWs) with trapped ions. In particular, we analyze in detail the limitations of the protocol of Travaglione and Milburn (PRA 2002) that has been implemented by several experimental groups in recent years. Based on the first realization in our group (PRL 2009), we investigate the consequences of leaving the scope of the approximations originally made, such as the Lamb–Dicke approximation. We explain the consequential deviations from the idealized QW for different experimental realizations and an increasing number of steps by taking into account higher-order terms of the quantum evolution. It turns out that these become dominant after a few steps already, which is confirmed by experimental results and is currently limiting the scalability of this approach. Finally, we propose a new scheme using short laser pulses, derived from a protocol from the field of quantum computation. We show that the new scheme is not subject to the above-mentioned restrictions, and analytically and numerically evaluate its limitations, based on a realistic implementation with our specific setup. Implementing the protocol with state-of-the-art techniques should allow for substantially increasing the number of steps to 100 and beyond and should be extendable to higher-dimensional QWs.

1. Introduction

Random walks are powerful models that allow to describe, understand and make use of stochastic processes occurring in a wide variety of areas [1, 2]. Models describing related processes in the quantum world are called quantum walks (QWs) [3].

An implementation of a discrete (-time and -space) random walk on a line requires two basic operations. The coin operation, with the random outcome of Heads or Tails, is followed by the shift operation to the left or right, depending on the outcome of the coin toss. After N steps the walker will therefore have followed randomly one out of many possible paths, with the probability for its location being given by a binomial distribution centered around the starting point. The average displacement of the walker, i.e. the standard deviation of that distribution, increases with the square root of N . The quantum mechanical version replaces the probabilistic coin toss by a deterministic operation. It prepares the quantum coin in an (equal) superposition of Heads and Tails. As a consequence, the walker performs the conditional step in both directions simultaneously. The walker follows all paths during this deterministic (and thus reversible) process, allowing for constructive and destructive interferences at subsequent crossings. The probability distribution of the position of the walker is due to these interferences substantially different from a binomial one. In particular, the average displacement of the walker scales linearly in N .

Quantum walks have been thoroughly investigated theoretically and several applications for QWs have been proposed, for example in terms of quantum computing [4]. Many classical algorithms in computer science make use of random walks for sampling purposes. Algorithms of that kind might get substantially speeded up by quantum versions of the random walk, where all possible paths are tested in parallel, potentially providing a similar gain as the prominent example of Grover's search algorithm [5]. In addition, QWs can be interpreted as the one-particle sector of a quantum cellular automaton, which is a fundamental model of a quantum computer [6]. Furthermore it has been shown that QWs themselves are suitable for universal quantum computation [7] and different aspects of quantum information processing [8, 9, 10].

In a different context, QWs can be exploited as prototype models for intriguing transport processes in nature. One examples is the energy transfer in photosynthesis with an efficiency of close to 100% [11, 12], a performance that is not achievable classically. Other examples are the creation of molecules in interacting QWs [13] and effects like Anderson localization and diffusive scaling in disordered QWs [14, 15]. Here, QWs might be suited for experimental quantum simulations to provide deeper insight into complex quantum dynamics. Additionally, even relativistic effects can be considered [16].

Promising attempts at their implementation have been performed for the discrete and the continuous versions of QWs. Important aspects of QWs have been realized in a nuclear magnetic resonance experiment [17] using the internal degrees of freedom of molecules to span the coin and position space. An implementation based on neutral

atoms in an optical lattice [18, 19] has resulted in an experiment [20] where the lattice sites in a standing wave of light span the position space of the walker/atom, two electronic states encode the two coin states and a state-dependent optical force provides the conditional shift. Other proposals consider an array of microtraps illuminated by a set of microlenses [21], Bose–Einstein condensates [22] and atoms in cavities [23]. Photons have mimicked single walkers on the longitudinal modes of a linear optical resonator [23] and in a loop of a split optical fibre [24]. Single [25] and two time-correlated photons [26, 27] have recently been travelling and interfering in a lattice of optical waveguides. Travaglione and Milburn [28] proposed a scheme for trapped ions to transfer the high operational fidelities [29] obtained in quantum information processing into the field of QWs. While coin states and steps are operated similar to the atoms in the optical lattice, the position is encoded in the motional degree of freedom of the ion(s), which oscillate in a quantized harmonic trapping potential. The proof-of-principle has been performed by our group by the implementation of a discrete, asymmetric QW of one trapped ion along a line in phase space [30]. Recently, the proposal has been theoretically refined [31] and experimentally extended to an increased number of steps [32].

All of the above-described systems and their related protocols of implementation are severely limited in the total number of steps due to a lack of operation fidelities or even fundamental restrictions. However, a larger number of precisely performed steps is the crucial prerequisite to exploit QWs for the envisioned applications. For the case of trapped ions, the limit of coherent displacements to states inside the Lamb–Dicke regime has already been foreseen [28], experimentally observed in a different context [33, 34], and confirmed by us [35] and others [32].

In this paper we substantially extend the description of the experimental implementation of the asymmetric QW with three steps [35]. We carefully analyze the effects that arise when approaching the fundamental limitations of the proposed protocol [28] after the related, severely restricted number of steps for different step sizes. We consider higher-order terms to the soon overstrained approximation building on the work of [33]. In parallel, we experimentally confirm the essentials by further investigating our results [35], which already lead into a regime where the refined theory is required. Finally, we develop a novel protocol for a QW, based on a scheme from the field of quantum information processing using photon kicks [36, 37], to overcome these restrictions and to allow in principle for hundred(s) of steps, extendable to QWs in higher dimensions.

The paper is structured as follows: In section 2 we give a theoretical description of the QW as it has been realized in our experiment, similar to the original proposal [28], and analyze issues concerning non-orthogonality of the position states. In section 3 we describe the experimental method of realizing the necessary operations of the QW and analyze the limitation of the position space to the LDR of the optical dipole force. In section 3.5 we describe the experimental methods of the ion state detection. In section 4 we describe the experimental procedure, in particular the determination of

the relevant parameters. In section 5 we summarize the results and the limitations of the implementation of the QW. Finally, in section 6, we propose the implementation of the shift operator with short laser pulses (photon kicks) and the extension to higher dimensions.

2. Theoretical considerations

In the following we give a theoretical description of the discrete QW on a line as it is realized in our proof-of-principle experiment for the first three steps.

Consider a Hilbert space vector

$$|\psi\rangle \in \mathbb{H} = \mathbb{H}_{\text{coin}} \otimes \mathbb{H}_{\text{motion}}. \quad (1)$$

\mathbb{H}_{coin} denotes the coin space with basis states

$$|H\rangle = \begin{pmatrix} 1 \\ 0 \end{pmatrix}, \quad |T\rangle = \begin{pmatrix} 0 \\ 1 \end{pmatrix}, \quad (2)$$

encoding the coin states, Heads and Tails. $\mathbb{H}_{\text{motion}}$ is the infinite dimensional phase space, related to a harmonic oscillator. We encode the discrete positions as coherent states

$$|\alpha_k\rangle = e^{-|\alpha_k|^2/2} \sum_{n=0}^{\infty} \frac{\alpha_k^n}{\sqrt{n!}} |n\rangle, \quad (3)$$

where $k \in \mathbb{Z}$ and $\alpha_k = k \cdot \Delta\alpha$ with $\Delta\alpha \in \mathbb{C}$. The states $|n\rangle$ denote the (orthonormal) Fock states. For the QW the distance $|\Delta\alpha|$ between neighbouring positions in phase space is of importance, whereas the argument of the complex number $\Delta\alpha$ can be chosen to be constant for all steps and therefore is irrelevant.

Concerning the notation of the position states, we will use the following convention. Ideally, the position states are coherent motional states $|\alpha_k\rangle$, as described above. In the experiment the position states will contain a small amount of motional squeezing (Sect. 4.1). These states will be denoted as $|\tilde{\alpha}_k\rangle$. Additionally, whenever necessary, we will distinguish between position states generated in a numerical simulation, $|\tilde{\alpha}_k^S\rangle$, and experimentally, $|\tilde{\alpha}_k^E\rangle$. Further, we will generally use the superindices S and E to distinguish between simulation and experiment, whenever necessary. For the simulation we will use 3SB (See sect. 3.4.2), if not stated differently.

Ideally, the initial state of the QW is chosen to be

$$|\psi_0\rangle = |T\rangle \otimes |\alpha_0 = 0\rangle. \quad (4)$$

Each step of the QW is described by the subsequent application of the coin operator C and the shift operator S . Thus the state after N steps is given by $|\psi_N\rangle = (S \cdot C)^N |\psi_0\rangle$.

The coin operator C is defined as

$$C = R\left(\frac{\pi}{2}, \phi\right) = \frac{1}{\sqrt{2}} \begin{pmatrix} 1 & e^{i\phi} \\ -e^{-i\phi} & 1 \end{pmatrix} \otimes \mathbf{1}_{\text{motion}}, \quad (5)$$

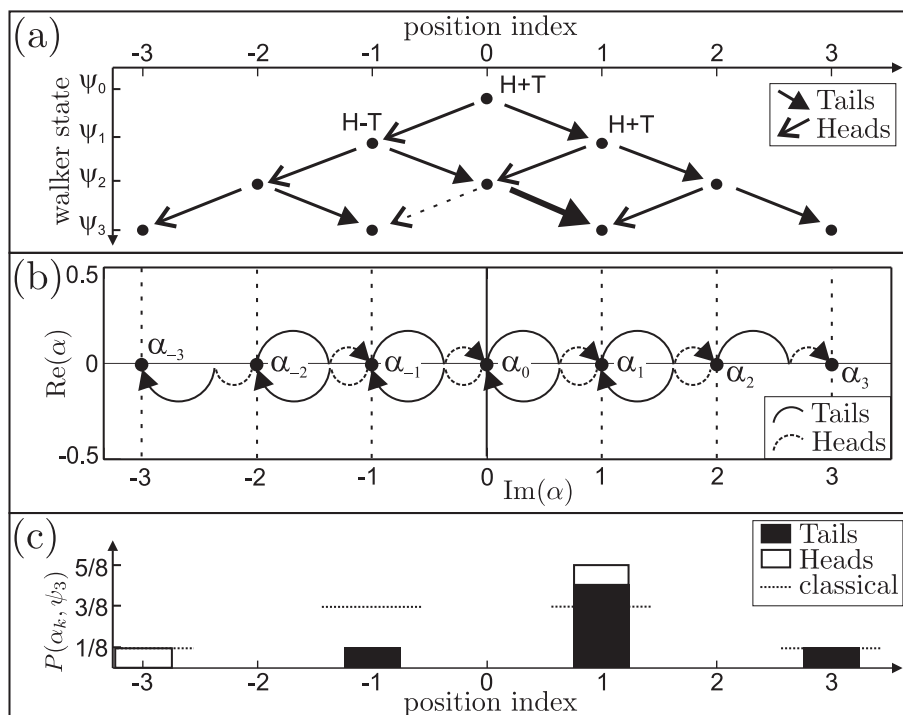


Figure 1. The asymmetric QW on a line. (a) Schematic of the QW. Starting at the position with index 0, the walker tosses a coin and does a shift to the position index 1 (−1) for the coin showing Tails (T) (Heads (H)). If the coin is in a superposition of T and H , the walker shifts into both directions simultaneously, taking the part related to T to position 1 and the one related to H to position −1. Further coin tosses from T (H) cause superposition states with different relative phases, that is, $H + T$ and $H - T$ respectively. The relative phases allow for interferences of the wave function between different paths. The first interference occurs during the third step, taking the walker from the state ψ_2 to ψ_3 . At position 0 the coin toss results in constructive (destructive) interference for T (H), illustrated by the bold (dashed) arrow for the subsequent shift. (b) We implement the QW with a trapped ion, where the position space is encoded into the co-rotating phase space ($\text{Re}(\alpha)$, $\text{Im}(\alpha)$) (23) of the axial normal mode of motion. The positions k are represented by coherent states $|\alpha_k\rangle$, which are aligned along a line in the co-rotating phase space. Two electronic (hyperfine) states of the ion encode the coin states. The transition from position $|\alpha_k\rangle$ to $|\alpha_{k\pm 1}\rangle$ is achieved via two subsequent displacements, each followed by a pulse exchanging the the coin states (See figure 9). (c) Probability distribution of the walker in position space after three steps, under the assumption that the position states are orthogonal. The black (white) filled boxes represent the contributions of the wave function related to $|T\rangle$ ($|H\rangle$). The asymmetry between the position state probabilities $P(\alpha_1, \psi_3) = \langle \psi_3 | (\mathbb{I} \otimes |\alpha_1\rangle \langle \alpha_1|) | \psi_3 \rangle$ and $P(\alpha_{-1}, \psi_3)$ is due to the interferences indicated via the bold and dashed arrows in (a).

according to

$$R(\theta, \phi) = \begin{pmatrix} \cos(\theta/2) & e^{i\phi} \sin(\theta/2) \\ -e^{-i\phi} \sin(\theta/2) & \cos(\theta/2) \end{pmatrix} \otimes \mathbb{I}_{\text{motion}}. \quad (6)$$

From the initial state $|\psi_0\rangle$, the operator C with ϕ being arbitrary, but equal for every application of C , leads to an asymmetric QW (Figure 1). A symmetric QW can be realized with the coin operator for the first step being $R(\pi/2, \phi)$ and for all following steps being $R(\pi/2, \phi + \pi/2)$ (with ϕ arbitrary). In that case, the first coin toss can be interpreted as the initialization of the coin state such that all following coin tosses act

symmetrically on it.

The shift operator S is defined as

$$S = |T\rangle\langle T| \otimes D(\Delta\alpha) + |H\rangle\langle H| \otimes D(-\Delta\alpha), \quad (7)$$

with $D(\Delta\alpha) = \exp(\Delta\alpha \cdot a^\dagger - \Delta\alpha^* \cdot a)$ being the displacement operator and a^\dagger, a the corresponding raising and lowering operators.

In contrast to a typical QW \ddagger the position states $|\alpha_k\rangle$ are not orthogonal. The step size $|\Delta\alpha|$ determines the overlap of the position states, $\langle\alpha_k|\alpha_l\rangle = \exp(-(k-l)^2|\Delta\alpha|^2/2)$. If the state of the walker after N steps is $|\psi_N\rangle = \sum_{k=-N}^N (c_k^T |T\rangle |\alpha_k\rangle + c_k^H |H\rangle |\alpha_k\rangle)$, the probability of finding the walker in position $|\alpha_L\rangle$ is given by

$$\begin{aligned} P(\alpha_L, \psi_N) &= \langle\psi_N| (\mathbf{1} \otimes |\alpha_L\rangle\langle\alpha_L|) |\psi_N\rangle \\ &= \left| \sum_{k=-N}^N c_k^H \cdot \langle\alpha_k|\alpha_L\rangle \right|^2 + \left| \sum_{k=-N}^N c_k^T \cdot \langle\alpha_k|\alpha_L\rangle \right|^2. \end{aligned} \quad (8)$$

Thus only if the step size $|\Delta\alpha|$ is large enough such that the overlap between different position states remains negligible, the above probability is given by the coefficients c_L^H and c_L^T only. In figure 2 the probability distributions after 100 steps for QWs with different step sizes $|\Delta\alpha|$ are illustrated. We find that for $|\Delta\alpha| \geq 2$, where the position states contain a negligible overlap of $|\langle\alpha_k|\alpha_{k+1}\rangle|^2 \leq e^{-4}$, the probability distribution shows the shape of an orthogonal QW [4]. For smaller values of $|\Delta\alpha|$ the probability distributions are smeared out due to the increased overlaps between the position states. As $|\Delta\alpha|$ approaches zero, the probability distribution approaches a Gaussian shape. The mean distance of the walker from the origin, which is given by the standard deviation

$$\sigma_N = \sqrt{\langle k^2 \rangle_N - \langle k \rangle_N^2} \quad (9)$$

with

$$\langle f(k) \rangle_N = \frac{\sum_{k=-N}^N f(k) \cdot P(\alpha_k, \psi_N)}{\sum_{k=-N}^N P(\alpha_k, \psi_N)} \quad (10)$$

for any function $f(k)$, grows slower with N for smaller values of $|\Delta\alpha|$. This is because the lower the value of $|\Delta\alpha|$, the less the shift operator S actually changes the state of the walker. However, for every realization of $|\Delta\alpha|$ the average distance of the walker from the origin scales linearly with the step number N , i.e. $\sigma_N \equiv v(\Delta\alpha) \cdot N$, after a certain number of steps, as depicted in figure 2b. The asymptotic scaling for the limit $|\Delta\alpha| \rightarrow 0$ has not been investigated yet.

In our experiment we set the step size to $|\Delta\alpha| \approx 1$. In this case the overlaps between the position states amount to $|\langle\alpha_k|\alpha_{k+1}\rangle|^2 = 1/e$. The characteristic of the probability

\ddagger In the sense that the position states are orthogonal, which has to our knowledge been assumed in the vast majority of publications concerning QWs, so far.

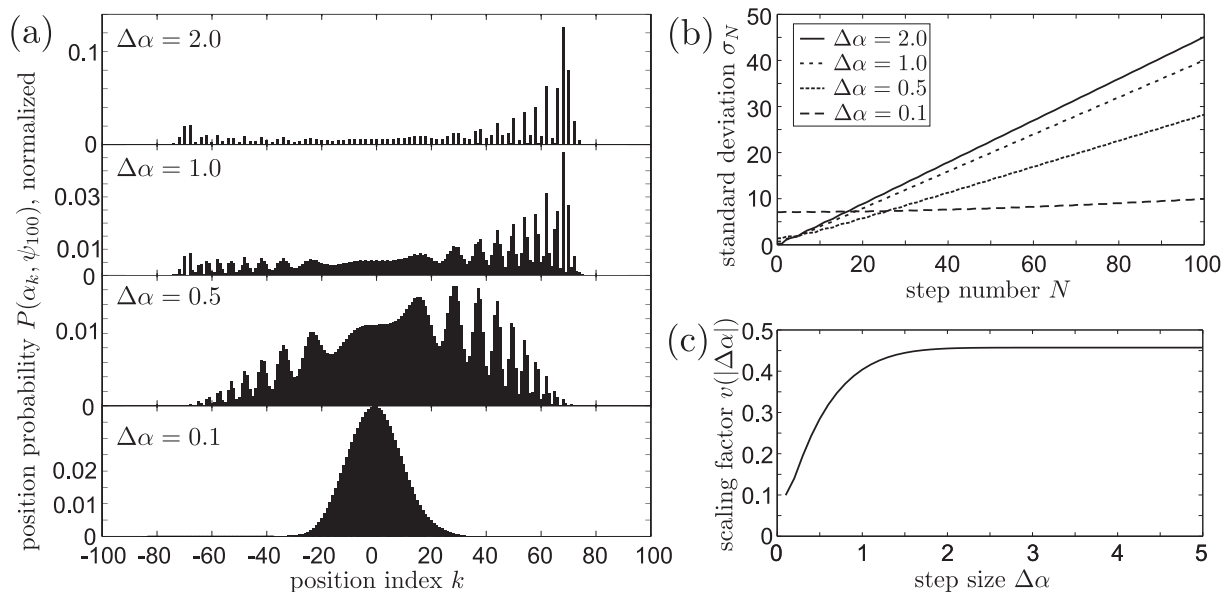


Figure 2. Characteristics of the probability distribution for asymmetric QWs of different step sizes $|\Delta\alpha|$. (a) Position probabilities $P(\alpha_k, \psi_{100})$ after $N = 100$ steps. The probabilities are normalized to $\sum_k P(\alpha_k, \psi_{100}) = 1$. For $|\Delta\alpha| \geq 2$ the position states are approximately orthogonal and therefore the probability distribution shows the shape of an orthogonal QW [4]. In particular, the probabilities for positions $|\alpha_k\rangle$ with odd index k vanish. For $|\Delta\alpha| = 1$ the probability distribution is smeared out and all position states are populated. However, the characteristic peaks around $k = 70$ are still prominent. For $|\Delta\alpha| = 0.5$ the probability distribution does not feature the main peak around $k = 70$ any more. For $|\Delta\alpha| = 0.1$ the probability distribution approaches a Gaussian shape. (b) Standard deviation σ_N (9) in dependence on N for QWs with different step sizes $|\Delta\alpha|$. After a few initial steps the standard deviation scales linearly in N , i.e. $\sigma_N = v(|\Delta\alpha|) \cdot N$. For $|\Delta\alpha| = 0.1$ already the initial state $|\psi_0\rangle$ of the walker is considerably spread out over the position states $|\alpha_k\rangle$ such that the standard deviation differs significantly from zero. The linear scaling becomes evident for $N \gtrsim 60$. (c) Scaling factor $v(|\Delta\alpha|)$ of the standard deviation for different step sizes $|\Delta\alpha|$. For $|\Delta\alpha| \geq 2$ the scaling factor is larger than 99% of the asymptotic value ($v(|\Delta\alpha| \rightarrow \infty) = 0.457$), which is the scaling of a QW with orthogonal position states. In our experiment we set the step size to $|\Delta\alpha| \approx 1$, which results in a scaling factor of 89% of the asymptotic value.

distribution after 100 steps (Figure 2a) is still close to that of $|\Delta\alpha| \geq 2$ and thus an orthogonal QW.

Ideally, with the initial state $|\psi_0\rangle$ and $\phi = 0$ (5) three steps of the asymmetric QW lead to the state

$$|\psi_3\rangle = \frac{1}{\sqrt{8}} |T\rangle \otimes \left(-2|\alpha_1\rangle + |\alpha_3\rangle - |\alpha_{-1}\rangle \right) + \frac{1}{\sqrt{8}} |H\rangle \otimes \left(|\alpha_{-3}\rangle + |\alpha_1\rangle \right). \quad (11)$$

The probabilities of finding the walker in the coin state $|H\rangle$ or $|T\rangle$ after three steps are given by $P_H(|\psi_3\rangle) = \langle\psi_3| (|H\rangle\langle H| \otimes \mathbf{1}) |\psi_3\rangle$ and $P_T(|\psi_3\rangle) = \langle\psi_3| (|T\rangle\langle T| \otimes \mathbf{1}) |\psi_3\rangle$. Their ratio

$$\frac{P_H(|\psi_3\rangle)}{P_T(|\psi_3\rangle)} = \frac{1 + e^{-8|\Delta\alpha|^2}}{3 - e^{-8|\Delta\alpha|^2}} \quad (12)$$

amounts to $\approx 1/3$ for $|\Delta\alpha| \geq 1$.

3. Implementation of the QW

3.1. System and definitions

For the experimental implementation we confine a single $^{25}\text{Mg}^+$ ion in a linear Paul trap [38]. The motional frequency related to the confinement in the axial direction of the trap is set to $\omega_z = 2\pi \cdot 2.13$ MHz and in the radial directions to $\omega_x \approx \omega_y \approx 2\pi \cdot 5$ MHz. We define two out of 12 electronic states of the hyperfine ground state manifolds [35] (Figure 4)

$$\begin{aligned} |H\rangle &\equiv |^2S_{1/2}, F = 2, m_F = 2\rangle, \\ |T\rangle &\equiv |^2S_{1/2}, F = 3, m_F = 3\rangle \end{aligned} \quad (13)$$

as the coin states. Further, we will use the state

$$|A\rangle \equiv |^2S_{1/2}, F = 2, m_F = -2\rangle \quad (14)$$

in the detection procedure. To lift the degeneracy within each hyperfine manifold, we apply a magnetic field inducing a Zeeman shift with an energy separation related to $\omega_{Zm} \approx 2\pi \cdot 3$ MHz between neighbouring states. The energy difference (including the hyperfine splitting) between $|H\rangle$ and $|T\rangle$ amounts to a frequency of $\omega_{coin} = 2\pi \cdot 1.77$ GHz.

Our realization of the QW consists of the application of a sequence of laser and radio-frequency (RF) pulses to (1) initialize the ion's electronic and motional state, (2) to implement the QW, and (3) to readout the final state via photon scattering. The experiments are repeated on the order of 1000 times for each set of parameters to obtain the required statistical relevance. A concise discussion of these tools in a generic context can be found in [39] and [40].

3.2. State initialization

At the beginning of each experiment the ion is prepared in the coin state $|T\rangle$ with a fidelity ≥ 0.99 by optical pumping [41], while the axial mode of motion is cooled close to the ground state by Doppler cooling ($\bar{n} \approx 10$) [42] and subsequent sideband cooling ($\bar{n} < 0.03$) [41]. The phase space of the axial mode of motion is used to encode the position of the walker. The radial modes are Doppler cooled ($\bar{n} \approx 4$), which enables a sufficient decoupling from the axial degree of freedom.

3.3. The coin operator

We drive coherent transitions between the coin states by applying a radio-frequency field (RF) for a duration t with frequency ω_{coin} (Figures 3 and 4) [39]. This implements the operator $R(\theta, \phi)$ (6) with $\theta = \Omega \cdot t$ and $\Omega = 2\pi \cdot 100$ kHz, the Rabi frequency of the transition. The phase ϕ for the first pulse of each experimental cycle is arbitrary. For every following pulse the phase ϕ is set identical with respect to the first pulse. The duration of one $R(\pi, \phi)$ -pulse amounts to $T_\pi = 5 \mu\text{s}$. The coherence time (drop of

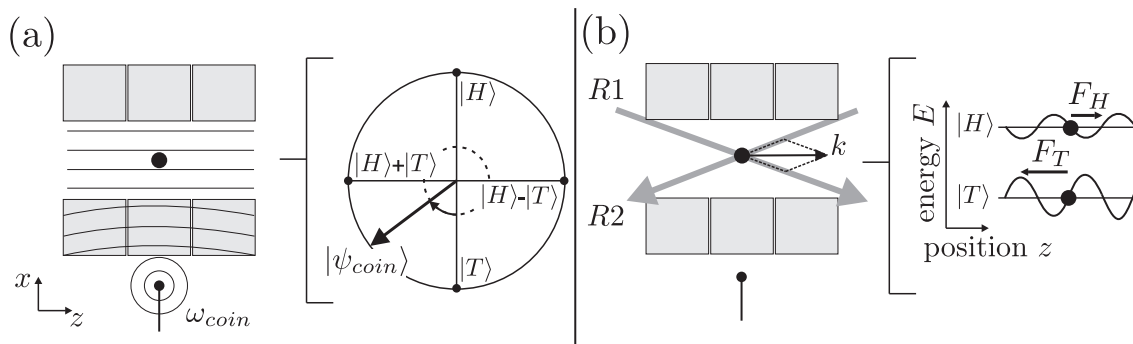


Figure 3. Schematic of the operations required for the implementation of the QW. (a) Implementation of the coin operator $R(\theta, \phi)$ (6). Left: The grey boxes represent a side view of two out of four electrodes of the Paul trap. The black dot between them depicts the trapped ion. We apply a radio frequency field (RF) via an antenna (below the grey boxes), driving coherent transitions between the coin states $|T\rangle$ and $|H\rangle$. The straight solid lines represent the phase fronts of the RF-field. Right: In our protocol of the QW we apply $R(\theta = \frac{\pi}{2}, \phi)$ -pulses ($\phi = \text{const.}$), rotating the state vector (Bloch representation) of $|\psi_{\text{coin}}\rangle$ by 90° from $|T\rangle$ ($|H\rangle$) to $|H\rangle + |T\rangle$ ($|H\rangle - |T\rangle$). (b) State dependent optical dipole force for the implementation of the shift operator S (7). Left: We apply two laser beams, $R1$ and $R2$, with a frequency difference $\omega_1 - \omega_2 = \omega_L = \omega_z - \delta$, perpendicular in polarization and beam direction. The effective wave vector is $\mathbf{k} = k\mathbf{e}_z$, pointing into the axial direction z . Right: This creates a walking standing wave and related state dependent ac-Stark shifts on the coin states $|H\rangle$ and $|T\rangle$, providing state dependent oscillating forces F_T (F_H) (solid sinusoidal lines) acting on the ion in the z -direction with frequency ω_L .

oscillation contrast below 50%) for the RF field exceeds one second [35]. The duration of a single experimental cycle (without initialization and detection) of the QW with three steps amounts to $150 \mu\text{s}$ (Figure 10). Therefore the dephasing of the coin remains small. Spin-echo sequences [39], which are included in the QW pulse sequence (Figure 10), further reduce the dephasing.

3.4. The shift operator

Ideally, we encode the positions of the QW into coherent motional states $|\alpha_k\rangle$ of the ion's axial harmonic motion. We manipulate the motion by implementing the shift operator S (7) via the application of a coin-state dependent optical dipole force (See figure 3b). In the following we describe this method and its limitations.

3.4.1. Experimental tools The initial motional state after sideband cooling is close to the ground state $|n=0\rangle$ ($\bar{n} < 0.03$). We apply a two-photon stimulated Raman transition between the coin states by applying two laser beams ($R1$, $R2$) (Figures 3b and 4), at a detuning of $\Delta = 2\pi \cdot 80 \text{ GHz}$ from the $P_{3/2}$ state manifold and a fixed phase relation [39]. The frequency difference between $R1$ and $R2$ amounts to

$$\omega_L = \omega_1 - \omega_2 = \omega_z - \delta, \quad (15)$$

with $\delta = 2\pi \cdot 100 \text{ kHz}$. The effective wave vector is $\mathbf{k}_1 - \mathbf{k}_2 = k\mathbf{e}_z$, pointing into the axial direction (Figure 3b). This allows for two-photon stimulated Raman transitions

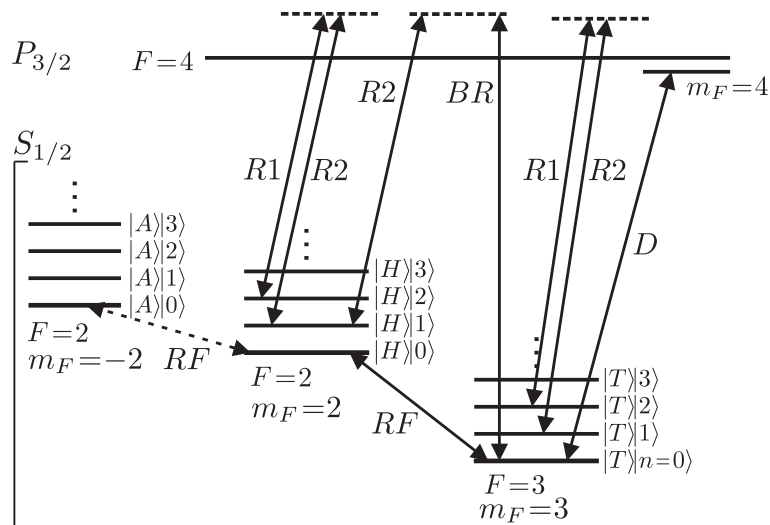


Figure 4. Schematic of the relevant electronic and some of the lowest motional energy levels (not to scale) of $^{25}\text{Mg}^+$ and the transitions used for the QW experiment. A magnetic field, pointing into the direction of the laser beam R1, provides a Zeeman splitting of the hyperfine levels and the quantization axis of the system. The coin states are encoded in $|^2S_{1/2}, F=3, m_F=3\rangle = |T\rangle$ and $|^2S_{1/2}, F=2, m_F=2\rangle = |H\rangle$. Laser D, driving a closed cycling transition, in good approximation independent of the motional level $|n\rangle$, is used for optically pumping the electronic state into $|T\rangle$, for Doppler cooling of all motional modes [42] and readout of the internal state (See sect. 3.5) [39]. The pair of laser beams BR and $R2$ is used to drive a two-photon stimulated Raman transition on the red sideband of the coin state transition for sideband cooling of the axiaconsequences of leaving the scope of the approximations originally used, such as the Lamb–Dicke regime.1 motional direction [41] and on the blue sideband (BSB, shown here) for the readout of the motional state (See sect. 3.5). The laser beams $R1$ and $R2$ drive a two-photon stimulated Raman transition providing the coin-state dependent optical dipole force (Figure 3b). Additionally we apply a RF to drive coherent transitions between electronic states, independent of the motional state (Figure 3a). With the RF we implement the coin operation and the transition via several steps from $|H\rangle$ to $|A\rangle = |^2S_{1/2}, F=-2, m_F=2\rangle$ required for the readout of the motional state (See sect. 3.5).

$|T\rangle|n\rangle \leftrightarrow |T\rangle|n+1\rangle$ and $|H\rangle|n\rangle \leftrightarrow |H\rangle|n+1\rangle$ ($\forall n$). In a simplified picture the two laser beams provide a walking standing wave causing a state dependent ac-Stark shift. This yields a coin-state dependent force (F_T, F_H), proportional to the spacial gradient of the walking wave and oscillating with frequency ω_L . The ratio of the forces acting on the coin states amounts to $F_H/F_T \approx -2/3$. The polarizations and intensities of the laser beams are adjusted such that the time-averaged ac-Stark shift for pulse durations $T \gg 0.5 \mu\text{s}$ is negligible [43]. Thus the application of the dipole force does not change the relation between the relative phase of the coin states and the phase of the RF, which implements the coin operator. The effective wavelength of the walking wave amounts to $\lambda \approx 200 \text{ nm}$. With the width of the axial ground-state wave function of $z_0 \approx 10 \text{ nm}$ this results in a Lamb–Dicke parameter of $\eta = z_0 \cdot 2\pi/\lambda = 0.31$ [39].

3.4.2. Description of the dynamics We consider the following Hamiltonian describing a two-level system coupled to a harmonic oscillator and interacting with a classical light

field [39]

$$\begin{aligned}
 \mathcal{H} &= \mathcal{H}_{\text{coin}} + \mathcal{H}_{\text{motion}} + \mathcal{H}_{\text{interaction}} \\
 &= \frac{\hbar}{2} \omega_{\text{coin}} \sigma_z + \hbar \omega_z (a^\dagger a + \frac{1}{2}) + \hbar \underline{\Omega}_D \cos(k \cdot z - \omega_L t + \phi_0) \\
 &= \frac{\hbar}{2} \omega_{\text{coin}} \sigma_z + \hbar \omega_z (a^\dagger a + \frac{1}{2}) + \frac{\hbar}{2} \underline{\Omega}_D \left(e^{i(\eta(a+a^\dagger) - \omega_L t + \phi_0)} + h.c. \right).
 \end{aligned} \tag{16}$$

where $\underline{\Omega}_D = \Omega_D (|T\rangle \langle T| - \frac{2}{3} |H\rangle \langle H|)$ with Ω_D the coupling factor and σ_z the Pauli z -matrix. The dynamics have been investigated for many applications in QIP [44, 45] (in the LDA, see below), for the simulation of nonlinear optics [46] and in the context of mesoscopic entanglement [33, 34]. In the interaction picture, with the free Hamiltonian being $\mathcal{H}_{\text{coin}} + \mathcal{H}_{\text{motion}}$, the interaction Hamiltonian can be written as

$$\begin{aligned}
 \mathcal{H}_I(t) &= \frac{\hbar}{2} \underline{\Omega}_D \otimes \sum_{m=0}^{\infty} \sum_{n=0}^{\infty} |m\rangle \langle m| e^{i\eta(a+a^\dagger)} |n\rangle \langle n| \\
 &\quad \times \left(e^{i((m-n)\omega_z - \omega_L)t + i\phi_0} + (-1)^{|m-n|} e^{i((m-n)\omega_z + \omega_L)t - i\phi_0} \right).
 \end{aligned} \tag{17}$$

We apply the dipole force with a small detuning of $\delta = \omega_z - \omega_L = 2\pi \cdot 100$ kHz, such that the terms corresponding to first-sideband transitions, $|n\rangle \leftrightarrow |n+1\rangle$, rotate slowest and thus dominate. However, we also consider contributions up to the third sideband, $|m-n| = 3$, an approximation we refer to as 3SB (Figures 6, 8 and 12).

When considering only the slowest rotating terms, i.e. applying the usual rotating-wave approximation (RWA), the interaction Hamiltonian is reduced to:

$$\begin{aligned}
 \mathcal{H}_I^{\text{RWA}}(t) &= \frac{\hbar}{2} \underline{\Omega}_D \otimes \sum_{n=0}^{\infty} \left(\langle n+1| e^{i\eta(a+a^\dagger)} |n\rangle e^{i(\delta t + \phi_0)} |n+1\rangle \langle n| \right. \\
 &\quad \left. - \langle n| e^{i\eta(a+a^\dagger)} |n+1\rangle e^{-i(\delta t + \phi_0)} |n\rangle \langle n+1| \right).
 \end{aligned} \tag{18}$$

For states with $k\sqrt{\langle z^2 \rangle} = \eta\sqrt{\langle (a+a^\dagger)^2 \rangle} \ll 1$, we can approximate $\langle n+1| e^{i\eta(a+a^\dagger)} |n\rangle \approx i\eta\sqrt{n+1}$ [40]. That is, the potential providing the dipole force changes linearly over the extension of the wave function. We can then simplify the interaction Hamiltonian to

$$\mathcal{H}_I^{\text{LDA}}(t) = \frac{\hbar}{2} \underline{\Omega}_D \otimes i\eta (a^\dagger e^{i(\delta t + \phi_0)} - a e^{-i(\delta t + \phi_0)}). \tag{19}$$

This is the Lamb–Dicke approximation (LDA) [39] or the linear approximation, respectively. In the following, we set $\phi_0 = 0$ and $\hbar = 1$.

Within the LDA, the time evolution operator is given by [47]

$$U(t) = |T\rangle \langle T| \otimes D(\alpha(t)) \cdot e^{i\Phi(\alpha(t), t)} + |H\rangle \langle H| \otimes D\left(-\frac{2}{3}\alpha(t)\right) \cdot e^{i\Phi\left(-\frac{2}{3}\alpha(t), t\right)}, \tag{20}$$

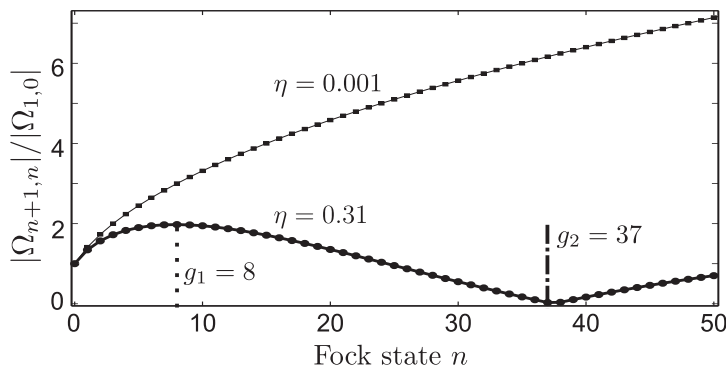


Figure 5. Normalized Fock-state transition rates $|\Omega_{n+1,n}|/|\Omega_{1,0}| = |\langle n+1 | \exp(i\eta(a + a^\dagger)) | n \rangle|$ (18) for a Lamb–Dicke parameter $\eta = 0.31$ (experimental value) and $\eta = 0.001$ (deeply within the LDR). As long as $|\Omega_{n+1,n}|/|\Omega_{1,0}| \approx \eta\sqrt{n}$, the force is constant over the ion’s motional extension. The time evolution is then described by a displacement operator (20), preserving the shape of coherent states. As the motional amplitude $|\alpha| = \sqrt{\langle n \rangle}$ increases, the force starts to remarkably change over the oscillating range of the wave function leading to motional squeezing. The Fock state at which the matrix element is maximal, i.e. $n = 8 \equiv g_1$ for $\eta = 0.31$, can be considered as the threshold above which severe motional squeezing of coherent states starts. The motional amplitude does not increase by the application of a continuous detuned force (See figure 6). Motional states up to g_2 for $\eta = 0.31$ can be created - with an increasing amount of squeezing - by applying the dipole force resonantly (Figure 7) or by step-wise excitation (Figure 8).

which is a displacement operator $D(\alpha(t))$ with a phase factor, where the phase amounts to

$$\Phi(\alpha(t), t) = \text{Im} \left(\int_0^t d\tau \alpha^*(\tau) \frac{d\alpha(\tau)}{d\tau} \right). \quad (21)$$

The factor $2/3$ in the displacement operator for the Heads-part results from the difference of the state-dependent dipole force, $F_H/F_T = -2/3$ (See figure 3). The complex parameter appearing in the displacement operator and in the phase amounts to

$$\alpha(t) = \frac{\eta\Omega_D}{2} \cdot \int_0^t e^{i\delta t} dt = -i \frac{\eta\Omega_D}{2\delta} \cdot (e^{i\delta t} - 1) \quad (22)$$

and corresponds to a circular trajectory in a co-rotating phase space, given by the interaction picture as

$$\begin{pmatrix} \text{Re}(\alpha(t)) \\ \text{Im}(\alpha(t)) \end{pmatrix} = \begin{pmatrix} \cos(\omega_z t) & \sin(\omega_z t) \\ -\sin(\omega_z t) & \cos(\omega_z t) \end{pmatrix} \begin{pmatrix} \frac{1}{2z_0} \langle z \rangle (t) \\ z_0 \langle p \rangle (t) \end{pmatrix}, \quad (23)$$

with $\langle z \rangle (t)$ and $\langle p \rangle (t)$ the expectation values of position and momentum.

For each coin state, the motional wave function is coherently displaced along a circular trajectory in the co-rotating phase space (Figure 6). The circular shape of the trajectory is caused by the dipole force being applied with a detuning δ relative to the oscillator frequency. Thus the relative phase between dipole force and oscillation of the ion evolves in time as $\phi_D(t) = \delta \cdot t$. After a duration of $T_\pi = \pi/\delta$ of driving the motional state and increasing its amplitude, the relative phase amounts to $\phi_D(T_\pi) = \pi$ and

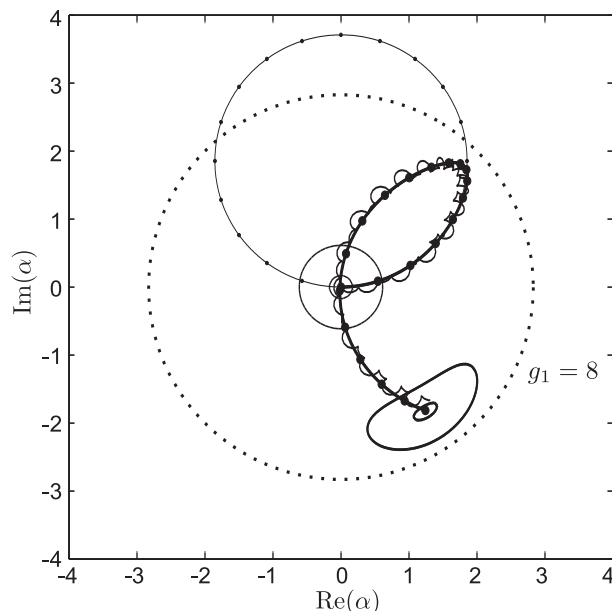


Figure 6. Numerical simulation of the ion's trajectory in co-rotating phase space (23) driven by the dipole force for the three relevant approximations 3SB (17), RWA (18) and LDA (19). The initial state is at the origin ($|\alpha_0 = 0\rangle$). The thin concentric lines represent contours of its Wigner function W (at $W_{>} = 0.6$ and $W_{<} = 0.3$). The bold dotted line represents g_1 (Figure 5). The thin circular trajectory with dots represents the result of the simulation within the LDA. The dots on the trajectory depict the positions after $t = 0, 0.5, \dots, 10$ μs . The final state, reached after $T_{2\pi} = 2\pi/\delta = 10$ μs , equals the initial one, up to a phase factor. The bold trajectory represents the result within the RWA, taking nonlinearities of the dipole force into account (Figure 5). The dots on the trajectory again depict the position at the times $t = 0, 0.5, \dots, 10$ μs . Starting from the origin, the trajectory is identical to the one within the LDA. In the vicinity of g_1 the trajectories start to deviate. The acceleration of the ion ceases at a certain amplitude, the state gets squeezed and then returns to the origin after a duration shorter than $T_{2\pi}$. The spiraling trajectory, which follows the one within the RWA, represents the results within 3SB. Here terms of higher frequencies in the Hamiltonian are taken into account. The final Wigner function is almost identical to the one in the RWA and therefore not shown. Parameters: $\Omega_D = 2\pi \cdot 1.2$ MHz, $\omega_L = 2\pi \cdot 2.03$ MHz, $\omega_z = 2\pi \cdot 2.13$ MHz, $\eta = 0.31$, $t \in [0, 10]$ μs .

therefore the dipole force starts to decelerate the oscillation of the ion. After a duration of $T_{2\pi} = 2\pi/\delta$ the coherent state returns to its initial location in the co-rotating phase space. The total acquired phase of the motional state, which equals the enclosed area of the trajectory [44], amounts to

$$\Phi_T = \pi \left(\frac{\eta \Omega_D}{2\delta} \right)^2 \quad (24)$$

for $|T\rangle$ and $\Phi_H = (4/9) \cdot \Phi_T$ for $|H\rangle$.

The nonlinearity of the potential causing spatial variations of the dipole force can be described by the absolute values of the transition matrix elements, i.e. $\Omega_{n+1,n} = \langle n+1 | \exp(i\eta(a+a^\dagger)) | n \rangle$ (Figure 5). For small Fock state numbers n they remain close to the approximative results within the LDA (where the potential is linear in z). Close to $n = 8 \equiv g_1$ (for $\eta = 0.31$) they start to significantly deviate from that approximation.

In particular, the transition matrix elements feature a maximum value at g_1 . The excitation of motion via the dipole force ceases at $n = 37 \equiv g_2$, due to $|\Omega_{38,37}| \approx 0$. It therefore represents an upper bound for the motional excitation with a dipole force applied close to resonance. (Applying the dipole force with a frequency $\omega_L = 2 \cdot \omega_z$ would allow populating higher Fock states, but since the overall time evolution is then described by a squeezing operator, it cannot be used for the implementation of a QW based on coherent displacements, following reference [28].)

Figure 6 presents the results of our numerical simulations of the time evolution, comparing the three different approximations 3SB, RWA and LDA. Starting in the motional ground state, the trajectory in the co-rotating phase space first follows the circular evolution, as long as the amplitude remains small, i.e. $\langle n \rangle < g_1$. This regime can be well described by the LDA (with the driving potential being linear in z). As the amplitude of the motional state approaches g_1 , the driving potential becomes sufficiently nonlinear to severely affect the subsequent evolution. The amount of displacement per time interval is substantially reduced, as the transition rates $|\Omega_{n+1,n}|$ decrease for $n \geq g_1$, such that the trajectory remains in the vicinity of g_1 . At this point motional squeezing occurs. The probability distribution of the wave function in the Fock state basis becomes narrower than Poissonian, which results in a squeezed shape of the corresponding Wigner function. The relative phase between the dipole force and the oscillation of the ion changes faster than in the linear case. Thus the squeezed wavefunction reaches the origin of the phase space after a time significantly shorter than $2\pi/\delta$. The dependence of the return time and the amount of squeezing on the maximal motional amplitude severely affect an implementation of a QW with position states outside the *LDR*, following the scheme described in reference [28]. However, in section 6 we propose an alternative protocol for the implementation of the shift operator that circumvents this restriction. The faster rotating terms, which are taken into account in the 3SB approximation, cause additional modulations of the trajectory with low amplitudes and high frequencies $(2\omega_z + \delta)$ and $(3\omega_z + \delta)$, respectively.

Further motional excitation (up to g_2) can be realized either by applying the dipole force resonantly (Figure 7) [46], or by the repeated off-resonant application of a weak dipole force with duration π/δ and constant time delays between the pulses (Figure 8). However, in either way severe motional squeezing occurs as the amplitude approaches and becomes larger than g_1 .

3.4.3. Implementation of the shift operator We implement several shifts into a certain direction in the co-rotating phase space by a synchronized application of dipole force pulses. Switching the dipole force is realized by acousto-optical modulators, refracting the laser beams *R1* and *R2* into the Paul trap [39]. As the laser is continuously on during the whole experiment, the phase relation between the dipole force and the motion of the ion continuously evolves in time as $\phi_D(t) = \delta \cdot t$, even when the optical dipole force is switched off. Therefore, after the first pulse of the dipole force, the relative phase $\phi_D(t)$ and thus the direction of the displacement caused by the following dipole force pulse

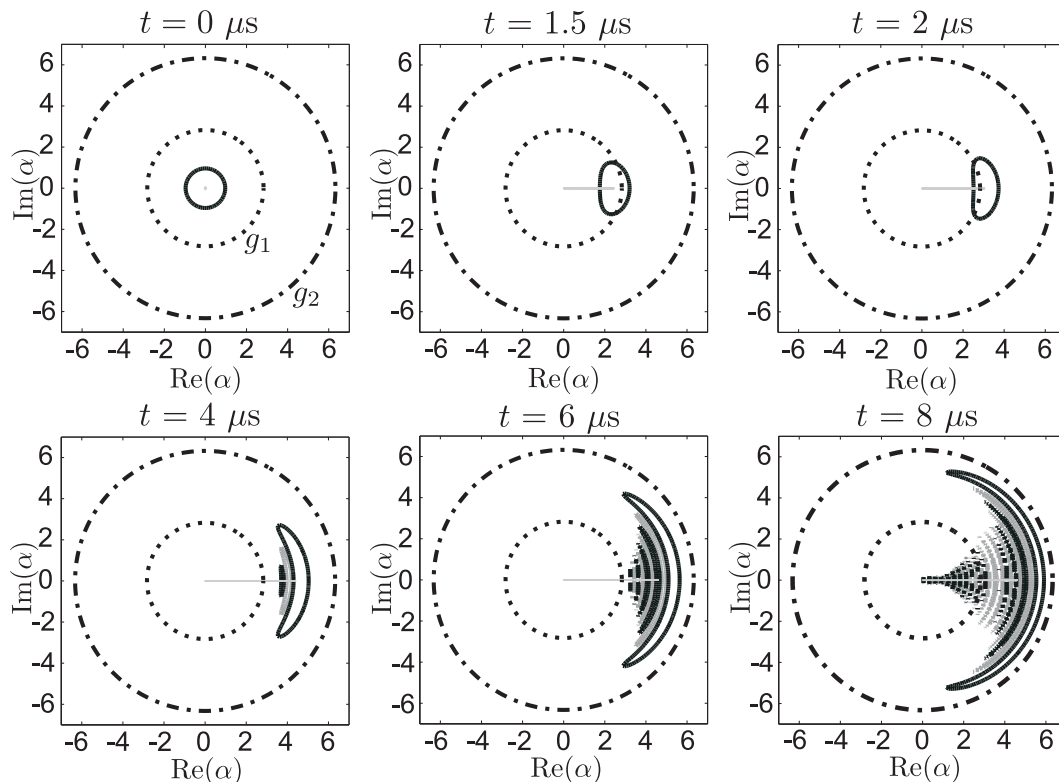


Figure 7. Numerical simulation (3SB) of a resonant ($\delta = 0$) excitation from the motional ground state, trajectory (grey horizontal line) and contours of the Wigner function W (black: $W = 0.1$, grey: $W = -0.1$) for increasing durations $t = \{0, 1.5, 2, 4, 6, 8\} \mu\text{s}$. Starting from the ground state, the dipole force continuously displaces the ion in good approximation to coherent states along the real axis up to g_1 (dotted circle). Further excitation comes along with severe motional squeezing. Amplitudes higher than g_2 are not considerably populated, due to the almost vanishing matrix element $\Omega_{37,38}$ at g_2 (dash-dotted circle) (Figure 5). As a consequence, at g_2 the wave function gets reflected in the sense that the amplitude gets decreased again. The interference of the accelerated and the decelerated (reflected) part of the wave function is resembled in the Wigner function, which shows concentric lines of positive and negative value in the populated area of the rotating phase space. Parameters: $\Omega_D = 2\pi \cdot 2.0$ MHz, $\omega_L = \omega_z = 2\pi \cdot 2.0$ MHz, $\eta = 0.3$.

depends on the intermitted delay. We apply pulses of the duration $T_D^{QW} \approx \pi/\delta = 5 \mu\text{s}$ and mutual delays that concatenate the displacements along a line in the co-rotating phase space (Figure 8).

However, the motional states corresponding to $|H\rangle$ and $|T\rangle$ acquire different phase factors Φ_H , Φ_T (24) during each displacement. To compensate these coin-state dependent phases, we implement the shift operation of the QW as a *combined pulse*, which consists of two dipole force pulses, each followed by an $R(\pi, 0)$ -pulse (Figure 9). In this scheme each coin state acquires the sum of the phase factors, $\Phi_T + \Phi_H$, which therefore turns into a global phase factor not affecting the QW. A schematic of the overall pulse sequence for the QW is depicted in figure (10).

For the implementation of the QW the following is crucial. After a step fulfilling the operation $|T\rangle |\tilde{\alpha}_k\rangle \rightarrow |T\rangle |\tilde{\alpha}_{k+1}\rangle$, the subsequent coin toss and shift operation have

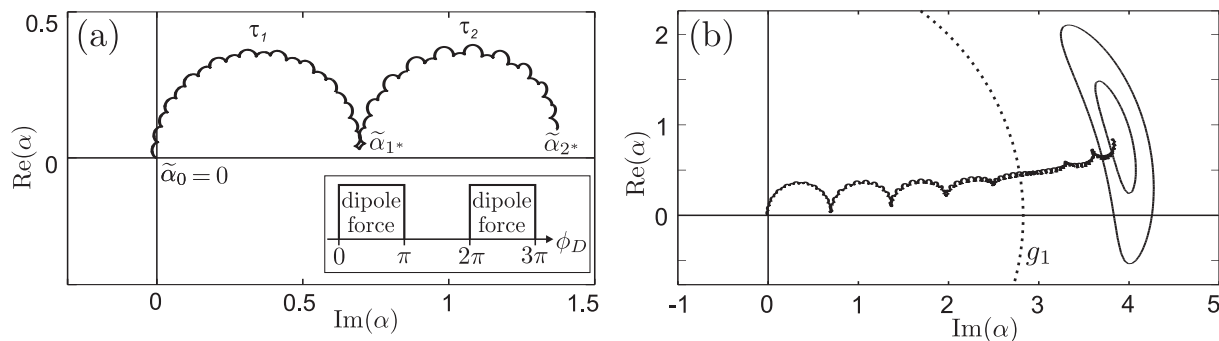


Figure 8. Numerical simulation (3SB) of the ion's trajectory in the co-rotating phase space during a stepwise excitation. (a) The first dipole force pulse (inlay) displaces the ion from the ground state to $|\tilde{\alpha}_{1*}\rangle$ (which is not the position state $|\tilde{\alpha}_1\rangle$, compare figure 9) along trajectory τ_1 . During the pulse the relative phase between dipole force and oscillator motion increases to $\phi_D = \pi$. The phase difference further increases after the dipole force is switched off (Sect. 3.4.3). After the duration $t = \pi/\delta$, it amounts to $\phi_D = 2\pi$. Applying now a second dipole force pulse (inlay) displaces the ion to $|\tilde{\alpha}_{2*}\rangle$ along trajectory τ_2 . (b) Stepwise excitation as described above, with eight steps, passing the threshold g_1 . As the state passes g_1 , the trajectory during each dipole force pulse follows the opposite direction of rotation (counter-clockwise). In this regime (in particular close to g_2) the time evolution can be approximated by a displacement operator as in (20) parametrized with $\alpha(-t)$ [46]. The contours of the final Wigner function show the strong motional squeezing. In addition, due to the dependency of the return time on the amplitude (Cf. Figure 6) the trajectory is on average not oriented along the horizontal axis. This is also the case in the protocol of the three-step QW (Figure 10), but does not affect its performance. Parameters: $\Omega_D = 2\pi \cdot 0.4$ MHz, $\omega_z = 2\pi \cdot 2.0$ MHz, $\delta = 2\pi \cdot 100$ kHz, $\eta = 0.3$.

to ensure the operation $|H\rangle |\tilde{\alpha}_{k+1}\rangle \rightarrow |H\rangle |\tilde{\alpha}_k\rangle$, i.e. the motional state $|\tilde{\alpha}_{k+1}\rangle$ must be transferred back to the previous state $|\tilde{\alpha}_k\rangle$. This must be fulfilled for all k simultaneously (See figure 1). In order to reach the state $|\tilde{\alpha}_k\rangle$, the duration T_D and detuning δ of the dipole force have to be adjusted properly (In the LDR to $T_D = \pi/\delta$), implementing semi-circular trajectories in the co-rotating phase space. But since the return time is reduced outside the LDR (Figure 6), the shift operation implements the transition from $|\tilde{\alpha}_{k+1}\rangle$ to some other state $|\tilde{\alpha}_{k_2}\rangle \neq |\tilde{\alpha}_k\rangle$. The reduced overlap $\langle \tilde{\alpha}_{k_2} | \tilde{\alpha}_k \rangle < 1$ leads to reduced interference during the succeeding coin toss (Figure 1).

In principle the shift operator can alternatively be implemented by the dipole force on resonance ($\delta = 0$). However, in that case small variations of ω_L and ω_z have a much stronger influence than in the detuned case. This can be seen by comparing the difference in displacement, i.e. $|\alpha(\delta, t) - \alpha(\delta + \epsilon, t)|$, for a fixed duration t and a fixed difference in the detuning, ϵ , using (22) for different values of δ , where $\alpha(\delta, t)$ fulfills equation (22) for the detuning δ .

3.5. State readout

The state after three steps of the QW is

$$|\tilde{\psi}_3\rangle = \frac{1}{\sqrt{2}} (|T\rangle |M_T\rangle + |H\rangle |M_H\rangle), \quad (25)$$

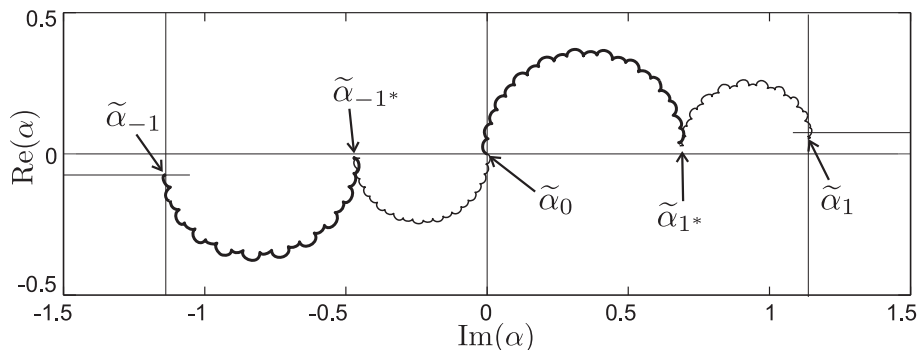


Figure 9. Numerical simulation (3SB) of the trajectories related to the ion's coin states $|T\rangle$ (bold trajectory) and $|H\rangle$ (thin trajectory) during step 1 of the QW (Figure 10). After the coin operation the ion's state is $|\psi\rangle = (|T\rangle + |H\rangle)|\tilde{\alpha}_0\rangle$ (where $|\tilde{\alpha}_k\rangle$ denotes the possibly slightly squeezed version of $|\alpha_k\rangle$). The shift operation S is implemented by a *combined pulse*. The first dipole force pulse displaces the motional state related to $|T\rangle$ ($|H\rangle$) to $|\tilde{\alpha}_{1^*}\rangle$ ($|\tilde{\alpha}_{-1^*}\rangle$). As the forces are of different amplitudes, the two different trajectories lead to different phase factors, related to Φ_T , Φ_H (24). Subsequently the coin states are exchanged via an $R(\pi, 0)$ -pulse without affecting the motional states and after a specific waiting duration (Figure 10) a second dipole force pulse is applied, displacing the motional states to $|\tilde{\alpha}_{-1}\rangle$ ($|\tilde{\alpha}_1\rangle$). A second $R(\pi, 0)$ -pulse exchanges the coin states again, such that the resulting state of the ion is $|\psi_1\rangle = \exp(i(\Phi_T + \Phi_H)) \cdot (|T\rangle|\tilde{\alpha}_1\rangle + |H\rangle|\tilde{\alpha}_{-1}\rangle)$, accumulating only a global phase during the shift operation. The combined-pulse scheme further provides equal step distances in both directions. Parameters: $\Omega_D = 2\pi \cdot 0.24$ MHz, $\omega_z = 2\pi \cdot 2.13$ MHz, $\delta = 2\pi \cdot 100$ kHz, $\eta = 0.31$.

with $|M_T\rangle = \sum_{k=-3}^3 c_k^T |\tilde{\alpha}_k\rangle$ and $|M_H\rangle = \sum_{k=-3}^3 c_k^H |\tilde{\alpha}_k\rangle$ (Cf. (11)). The basics for the readout are state-of-the-art techniques in quantum information processing with trapped ions [48, 39].

We readout the coin state by driving the cycling transition $|T\rangle|n\rangle \rightarrow |2P_{3/2}, F=4, m_F=4\rangle|n\rangle$ (Figure 4) for a duration of 20 μ s and detect scattered photons with a photomultiplier. This transition is in good approximation independent of the motional state. The average number of detected photons is proportional to the probability $P_T(\tilde{\psi}_3)$, related to the coin state $|T\rangle$ [39]. The probability $P_H(\tilde{\psi}_3)$ is accessible via the application of a $R(\pi, 0)$ -pulse before the coin-state detection.

To characterize the motional states of $|\tilde{\psi}_3\rangle$ we determine the position-state probabilities $|c_k^T|^2$ and $|c_k^H|^2$. To analyze $|T\rangle|M_T\rangle$, we isolate the other part, $|H\rangle|M_H\rangle$, by transferring $|H\rangle|M_H\rangle \rightarrow |A\rangle|M_H\rangle$ using appropriate RF pulses (Figure 4). The part $|A\rangle|M_H\rangle$ of the ion's state is not affected by the subsequent operations. We then apply a two-photon stimulated Raman transition $|T\rangle|n\rangle \leftrightarrow |H\rangle|n+1\rangle$ ($\forall n$) using the lasers BR and $R2$ (Figure 4), with a frequency difference of $\omega_L = \omega_{coin} + \omega_z$ (BSB) for a variable duration t_{BSB} [39]. The corresponding Rabi frequency for each n is proportional to $\Omega_{n+1,n}$ (Figure 5). Finally, we apply the coin-state detection, as described above. The average number of detected photons is proportional to the probability [39]

$$P_T(t_{BSB}) = \frac{1}{2} \left(1 + \sum_{n=0}^{\infty} |a_n^T|^2 \cdot \cos(\Omega_{n+1,n} \cdot t_{BSB}) e^{-\gamma \cdot t_{BSB}} \right), \quad (26)$$

with $a_n^T = \langle n|M_T\rangle$ the coefficients of $|M_T\rangle$ in the Fock state basis. The damping

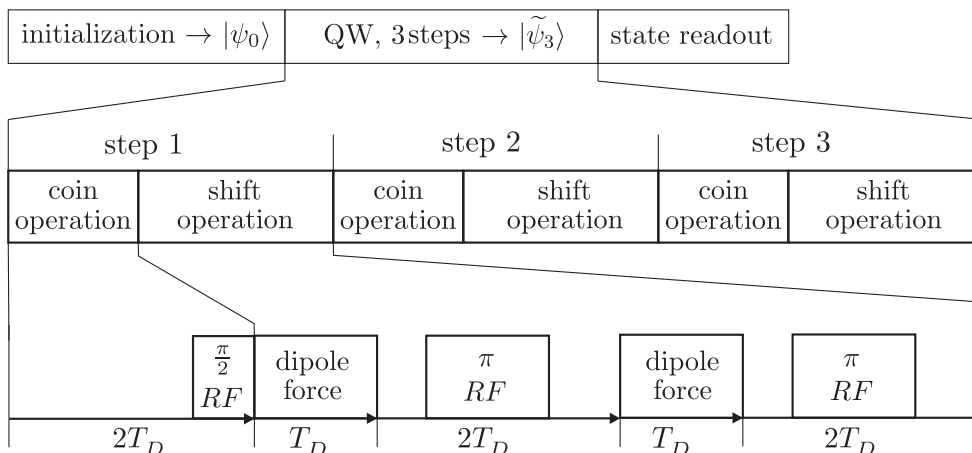


Figure 10. Schematic of the pulse sequence for the implementation of three steps of an asymmetric QW. The first line (top) illustrates the overall pulse sequence for one experimental cycle, in chronological order from left to right. We initialize the ion in the state $|\psi_0\rangle = |T\rangle|\alpha_0\rangle$. Then we apply the pulse sequence for the QW, creating the state $|\tilde{\psi}_3\rangle$ (25), and finally a pulse sequence to readout the coin or motional state (Sect. 3.5). The pulse sequence for the QW consists of three subsequent applications of coin C (Figure 3) and shift S (Figure 9) operations, implementing the three steps of the QW as illustrated in the second line. The third line depicts the pulses implementing one coin and one shift operation. The phase ϕ (not depicted) is equal for every RF pulse (Sect. 3.3). The sequence of all RF pulses incorporates a spin-echo scheme, reducing dephasing of the coin states. A symmetric QW can be implemented with the same scheme, but with the phase of the initial RF pulse differing by $\pi/2$ from the (equal) phases of all other RF pulses. The timing of the pulses, in particular for the dipole force, is given by the parameter T_D , as illustrated in the bottom. It must be chosen such that the overlap of the interfering motional states (Figure 1) is maximal. The theoretical optimal value within the LDR would be $T_D = \pi/\delta$. We determine the optimal value of T_D , denoted as $T_D^{QW} \approx \pi/\delta$, experimentally to account for the nonlinearity of the dipole force as well as for experimental imperfections (Figure 12).

factor γ accounts for decohering effects, mainly of the BSB-operation [39]. A discrete Fourier transform of the function $P_T(t_{BSB})$ allows to access the Fock state probabilities $|a_n^T|^2 = |\sum_k c_k^T \langle n|\tilde{\alpha}_k\rangle|^2$.

We numerically simulate the QW and generate a corresponding function $P_T^S(t_{BSB})$ (where the index S denotes the result of the simulation), and optimize the parameters of the simulation in order to fit $P_T^S(t_{BSB})$ onto the experimental data, $P_T^E(t_{BSB})$ (indicated by the index E). The state $|\tilde{\psi}_3^S\rangle$, generated by the simulation, resp. the Fock-state probabilities of its motional parts, are fed into the algorithm for the discrete Fourier transform of $P_T^E(t_{BSB})$ to improve the convergence of the results. The Fock state probabilities $p_n(\tilde{\alpha}_k) = |\langle n|\tilde{\alpha}_k\rangle|^2$ of the position states $|\tilde{\alpha}_k\rangle$ are determined separately (Figure 11), using the same method.

To identify the position state probabilities $|c_k^T|^2$ from the Fock state probabilities of $|M_T\rangle$, in particular to distinguish between the coefficients related to $p_n(\tilde{\alpha}_k)$ and $p_n(\tilde{\alpha}_{-k})$, we additionally apply the motional-state readout to the shifted states $|\tilde{\psi}_3^+\rangle = S|\tilde{\psi}_3\rangle$ and $|\tilde{\psi}_3^-\rangle = S^{-1}|\tilde{\psi}_3\rangle$ (See (7) and figure 14), where S^{-1} is (up to a global phase) implemented by a proper timing of the corresponding dipole force pulses.

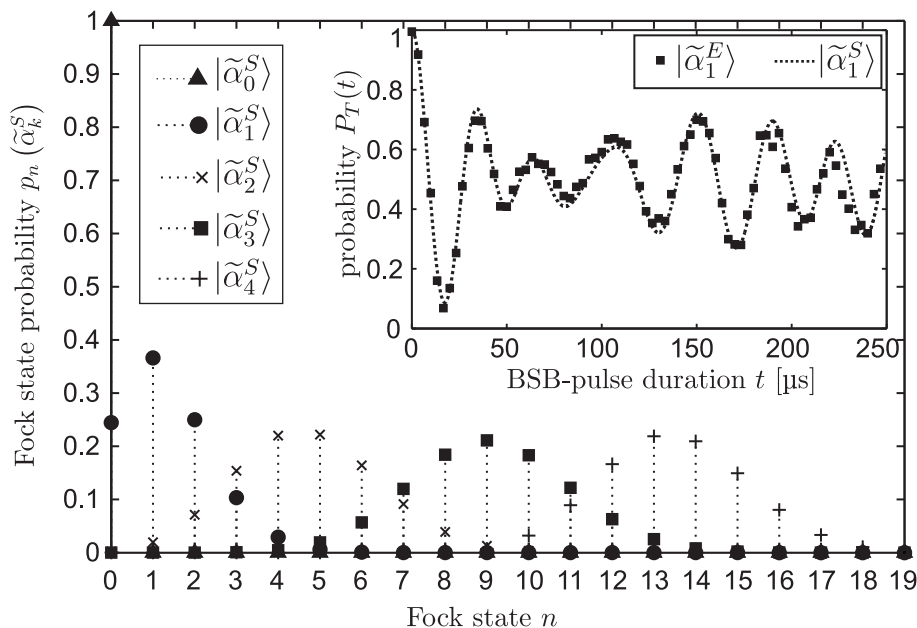


Figure 11. Fock state probabilities $p_n(\tilde{\alpha}_k^S) = |\langle n|\tilde{\alpha}_k^S\rangle|^2$ of the simulated (3SB) position states $|\tilde{\alpha}_k^S\rangle$ resembling the probabilities $p_n(\tilde{\alpha}_k^E)$ of the experimental position states $|\tilde{\alpha}_k^E\rangle$. Experimentally, we apply the shift operation S (Figure 9) k times (without coin operations) to the initialized ion and readout the motional state (Sect. 3.5). The inlay shows the coin state probability $P_T^E(t)$ (black squares) from the motional state readout of $|T\rangle|\tilde{\alpha}_1^E\rangle$, as an example. Each experimental data point represents the average of 3000 realizations. A simulation (3SB) of this procedure is optimized such that the values $P_T^S(t)$ (dotted line, cf. (26)) correspond to the experimental result for every position state $|\tilde{\alpha}_k^S\rangle$, as shown for $|\tilde{\alpha}_1^S\rangle$ in the inlay. The related expectation values of the position states in the Fock basis (main figure) are $\langle n\rangle_0^S = 0$, $\langle n\rangle_1^S = 1.33$, $\langle n\rangle_2^S = 4.71$, $\langle n\rangle_3^S = 9.08$, $\langle n\rangle_4^S = 13.50$. Their mutual overlaps amount to $|\langle \alpha_k^S|\alpha_{k+1}^S\rangle|^2 \approx 0.24$.

4. Experimental procedure

4.1. Calibration of the step size $|\Delta\alpha|$

Starting from the initial state $|\psi_0\rangle$ we apply 0 to 4 shift operations S with a dipole force duration of $T_D \approx \frac{\pi}{\delta}$, exciting the motion of the ion to one of the position states $|\tilde{\alpha}_k\rangle$. Then we readout the motional state to determine its Fock state probabilities $p_n(\tilde{\alpha}_k)$ and the expectation of the number operator $\langle n\rangle \equiv |\tilde{\alpha}_k|^2$. Small deviations of the dipole force duration (See next subsection) do not influence the probabilities significantly. We adjust the amplitude of the dipole force by adjusting the corresponding laser beam intensities to approximately meet the conditions $|\Delta\alpha| \geq 1$ and $|\tilde{\alpha}_3|^2 \equiv \langle \tilde{\alpha}_3|n|\tilde{\alpha}_3\rangle \leq 9$ (three well distinguishable position states within or close to the LDR). The Fock state expectation values of the position states amount to $\langle n\rangle_0 = \langle \tilde{\alpha}_0|n|\tilde{\alpha}_0\rangle = 0$, $\langle n\rangle_1 = 1.33$, $\langle n\rangle_2 = 4.71$, $\langle n\rangle_3 = 9.08$, $\langle n\rangle_4 = 13.50$. The outer position states $|\tilde{\alpha}_{\pm 3}\rangle$ and $|\tilde{\alpha}_{\pm 4}\rangle$ are not within the LDR. The step sizes therefore differ, reaching from $|\tilde{\alpha}_1\rangle - |\tilde{\alpha}_0\rangle = 1.15$ to $|\tilde{\alpha}_4\rangle - |\tilde{\alpha}_3\rangle = 0.66$. However, due to the motional squeezing the overlaps of all neighbouring states amount to $|\langle \tilde{\alpha}_k|\tilde{\alpha}_{k+1}\rangle|^2 \approx 0.24 < 1/e$, which corresponds to the overlap of coherent states with a step size of $|\Delta\alpha| > 1$ as assumed in the theory (See

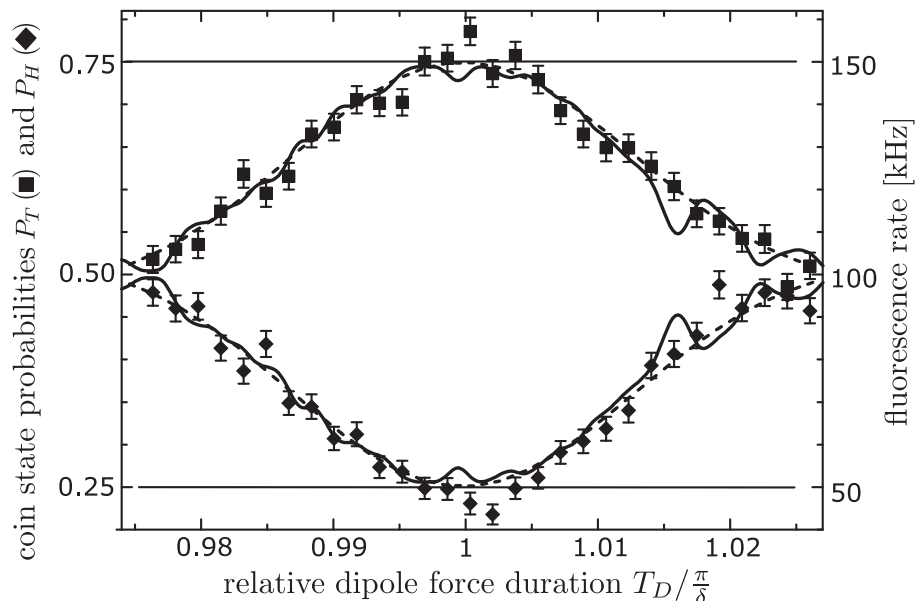


Figure 12. Coin state probabilities in dependence of the relative dipole force pulse duration ($T_D/(\frac{\pi}{\delta})$) after the application of the QW pulse sequence (Figure 10) to the ion in state $|\psi_0\rangle$, and the corresponding numerical simulations (solid line: 3SB, dashed line: RWA). Each data point represents the average of 1500 realizations. The maximum ratio $P_H/P_T = 1/3$ indicates the asymmetry due to interference (See figure 1). The corresponding dipole force duration, denoted as T_D^{QW} , is the optimal value to perform the QW. The precise value of T_D^{QW} depends on the detuning δ which is prone to slow drifts of the conditions of the experimental setup (on a time scale of a few hours, much longer than an experiment) and can be estimated to the required precision (for each experiment) by this method. For other values of T_D (i.e. 2% longer or shorter) the effect of the interference vanishes, since the shift operations of the pulse sequence do not lead to mutual overlaps of the related parts of the wave function. In this experiment the QW pulse sequence (Figure 10) contains waiting durations of $4T_D$ instead of $2T_D$, which increases the sensitivity of the interference to T_D and therefore allows for a more precise estimation of the optimal dipole force duration T_D^{QW} . The 3SB simulation (solid line), in contrast to the RWA simulation (dashed line), contains a high-frequency modulation of the coin state probabilities due to additionally modulated overlap of the interfering states caused by the spiralling trajectories during the displacements (Figure 6). This is however not yet resolved in the experimental data.

section 2). With $\delta = 2\pi \cdot 100$ kHz and $\eta = 0.31$ the corresponding coupling strength of the dipole force amounts to $\Omega_D = 2\pi \cdot 0.24$ MHz. The amplitude of the corresponding dipole force amounts to $F_T = (\hbar\eta\Omega_D)/(2z_0) = 2.54 \cdot 10^{-21}$ N inside the LDR.

To estimate the amount of motional squeezing (not affecting the fidelity of our results on the QW), we compute coherent states $|\alpha_k\rangle$ according to equation (3) with $\alpha_k \equiv \tilde{\alpha}_k$. We then compute their overlaps $F_k = |\langle \tilde{\alpha}_k | \alpha_k \rangle|^2$, which amount to $F_0 = 1.00$, $F_1 = 1.00$, $F_2 = 0.97$, $F_3 = 0.90$, $F_4 = 0.78$.

4.2. Calibration of the dipole force duration

The duration T_D of the dipole force pulses (and the related mutual delays, see figure 10) is a very sensitive parameter for the implementation of the QW. For a given detuning δ , T_D determines the relative direction of subsequent shifts in the co-rotating phase space.

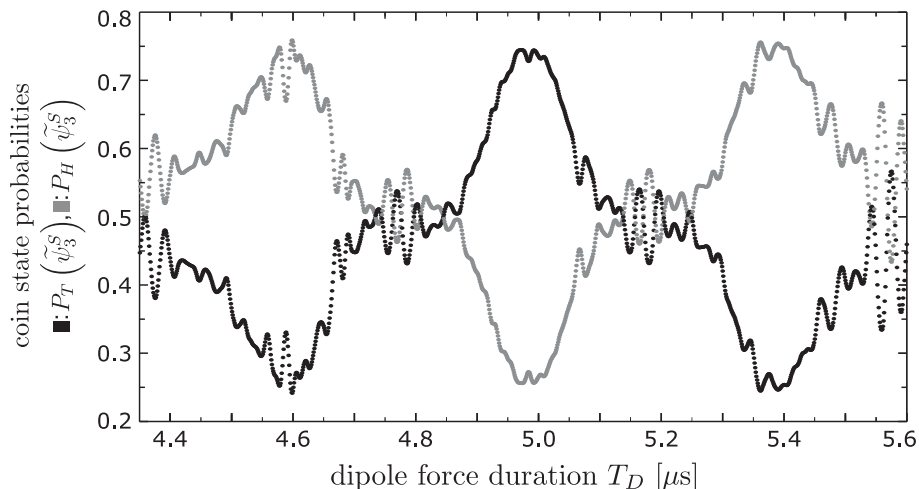


Figure 13. Numerical simulation (3SB) as depicted in figure 12 for extended values of T_D . Next to the largest difference between $P_T(\tilde{\psi}_3^S)$ and $P_H(\tilde{\psi}_3^S)$ at $T_D \approx 5.0 \mu\text{s} = \pi/\delta$, similar splittings occur at $T_D \approx 4.6 \mu\text{s}$ and $T_D \approx 5.4 \mu\text{s}$. These durations are such that subsequent shift operations displace into opposite directions in the co-rotating phase space. That is, at odd step numbers of the QW the shift operation acts as $|T\rangle|\alpha_k\rangle \rightarrow |T\rangle|\alpha_{k+1}\rangle$ and at even steps as $|T\rangle|\alpha_k\rangle \rightarrow |T\rangle|\alpha_{k-1}\rangle$, and analogously for $|H\rangle|\alpha_k\rangle$. This creates again a QW in which the shift directions of $|T\rangle$ and $|H\rangle$ are exchanged at each step.

By altering T_D we can control and maximize the overlap of the interfering parts of the wave function in the QW (Figure 1). We repeat the QW pulse sequence with increasing values of T_D (Figure 10) and acquire the coin-state probabilities P_T and P_H via the coin-state detection (Figure 12). The ratio P_T/P_H is an indicator for the amount of interference. If no interference occurs, it amounts to $P_T/P_H = 1$. We maximize the ratio by iterating to the optimal dipole force duration, denoted as $T_D^{QW} \approx \pi/\delta$. The nonlinearity of the dipole force, in particular the reduced return time discussed in sect. 3.4.2, leads to a deviation of T_D^{QW} from the duration π/δ , optimal within the LDA only. Additionally, this method is suitable to implicitly determine the detuning δ to the required precision.

As illustrated in figure 12, the maximum ratio of the measured probabilities amounts to $P_T/P_H \approx 3$, with the related dipole force duration being defined as T_D^{QW} . Averaged over 60000 measurements the coin state probabilities at this point amount to $P_T = 0.741 \pm 0.002$ and $P_H = 0.259 \pm 0.001$, which is close to the theoretical predictions 0.75 and 0.25 (Figure 1). At slightly different values of the dipole force duration, $T_D = T_D^{QW} \cdot (1 \pm 0.02)$ the coin state probabilities are approximately equal ($P_T/P_H \approx 1$), indicating that the overlaps and hence the interference of different parts of the wave function vanish.

The results of a numerical simulation of this procedure within 3SB are in good agreement with the experimental data (Figure 12). Additionally, the simulation shows similar splittings of the coin state probabilities at the dipole force durations $T_D = 4.6 \mu\text{s}$ and $T_D = 5.4 \mu\text{s}$, for $\delta = 2\pi \cdot 100 \text{ kHz}$ (Figure 13). These are QWs in which the step

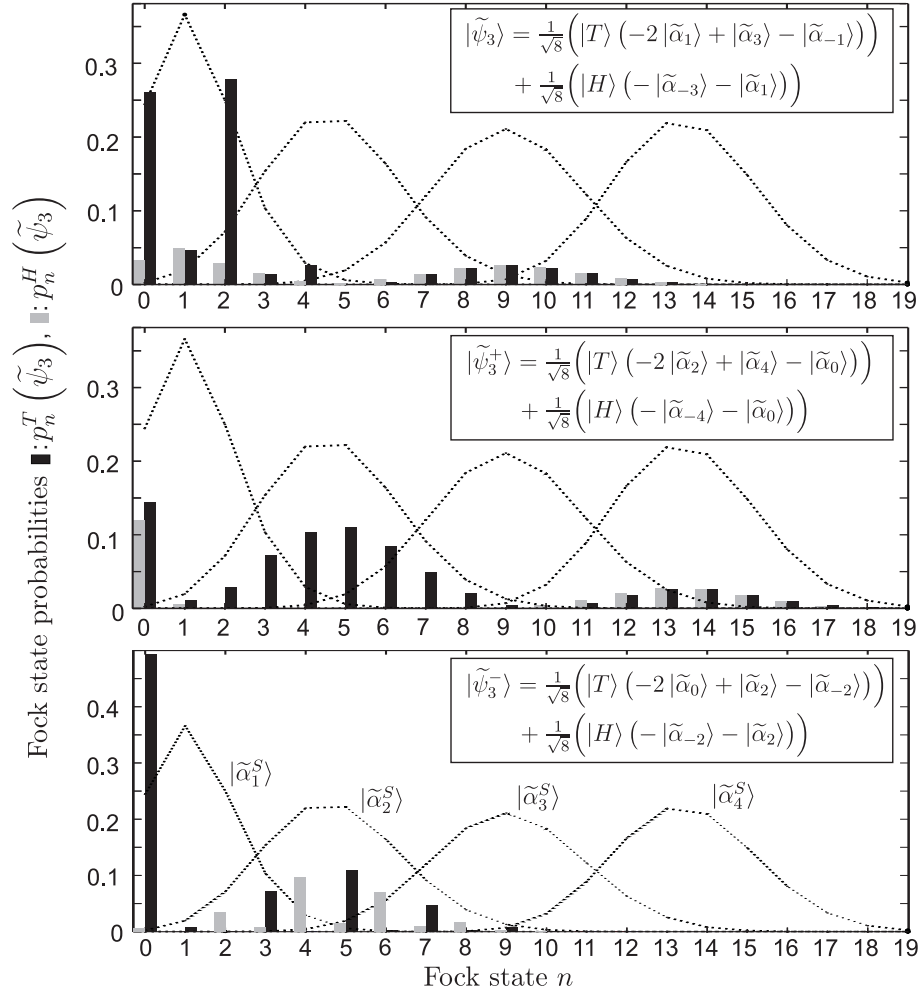


Figure 14. Fock state probabilities $p_n^T(\psi) = |\langle T | \langle n | \psi \rangle|^2$ and $p_n^H = |\langle H | \langle n | \psi \rangle|^2$ of the simulated QW state $|\tilde{\psi}_3^S\rangle$ (top), the shifted states $|\tilde{\psi}_3^{+,S}\rangle, |\tilde{\psi}_3^{-,S}\rangle$ (center, bottom) and of the position states $|\tilde{\alpha}_k^S\rangle$ (dotted lines), as in figure 11. All simulations are computed with equal parameters ($T_D^{QW} = 4.990 \mu\text{s}$ and the 3SB approximation). Each simulated state is in agreement with the corresponding experimental data, as exemplarily depicted in figure 11 (inlay). Top: $|\tilde{\psi}_3\rangle$ contains a superposition of $|\tilde{\alpha}_1\rangle$ and $|\tilde{\alpha}_{-1}\rangle$. This causes an interference (not related to the interference of the QW) in Fock space, resulting in high probabilities for even ($n = 0, 2, 4$) and low probabilities for odd Fock states. With the states $|\tilde{\psi}_3^{+,S}\rangle$ (center) and $|\tilde{\psi}_3^{-,S}\rangle$ (bottom), where the position occupations are shifted by one position, it is possible to distinguish the probabilities corresponding to $|\tilde{\alpha}_k\rangle$ and $|\tilde{\alpha}_{-k}\rangle$.

directions of $|T\rangle$ and $|H\rangle$ are exchanged at each step.

The simulation also shows a high frequent modulation of the coin state probabilities in dependence of T_D . This is due to the fast modulations of the trajectories in the rotating phase space, mainly caused by $|n+2\rangle \leftrightarrow |n\rangle$ -contributions of the dipole force (See figure 6).

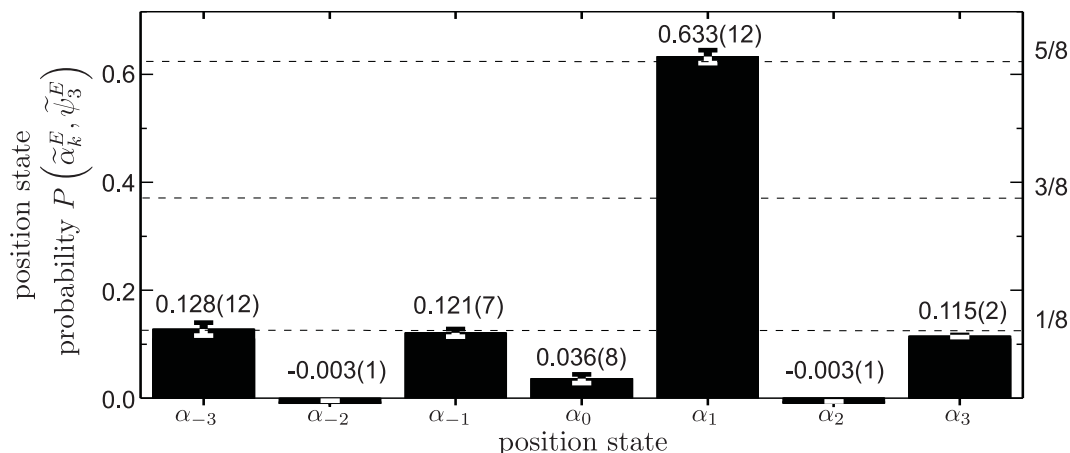


Figure 15. Position probabilities $P(\tilde{\alpha}_k^E, \tilde{\psi}_3^E)$ after three steps of the asymmetric QW. These are acquired by a discrete Fourier analysis of the data from the motional state detection (26) of the states $\tilde{\psi}_3^E, \tilde{\psi}_3^{+,E}, \tilde{\psi}_3^{-,E}$ (Cf. figure 14). The error bars represent the errors of the discrete Fourier analysis. The probabilities are in agreement with the theoretical values of an asymmetric QW (See figure 1). In particular the difference of the probabilities $P(\tilde{\alpha}_1^E, \tilde{\psi}_3^E)$ and $P(\tilde{\alpha}_{-1}^E, \tilde{\psi}_3^E)$ indicates the high fidelity of the implementation of the QW. The probabilities at the positions $|\tilde{\alpha}_{-2}^E\rangle, |\tilde{\alpha}_0^E\rangle$ and $|\tilde{\alpha}_2^E\rangle$ remain nonzero due to the overlaps with the neighbouring position states. The probabilities due to the overlaps have been subtracted, using the probabilities at $|\tilde{\alpha}_{\pm 1}^E\rangle$ and $|\tilde{\alpha}_{\pm 3}^E\rangle$ as a reference. Therefore the remaining nonzero values are an indicator for the error of the implementation and readout of the QW.

5. Experimental results and conclusion

We implement the QW pulse sequence (Figure 10) with the optimized dipole force duration T_D^{QW} (Figure 12) and apply the motional state readout (Sect. 3.5). The resulting Fock state probabilities from the corresponding simulation are illustrated in figure 14. To distinguish the position states $|\tilde{\alpha}_k\rangle$ and $|\tilde{\alpha}_{-k}\rangle$, which have the same Fock state probabilities, we also apply the motional state readout to the states $|\tilde{\psi}_3^+\rangle$ and $|\tilde{\psi}_3^-\rangle$, where after the QW pulse sequence an additional shift operation towards higher (lower) position states has been applied. The position state probabilities corresponding to the experimental data are illustrated in figure 15.

The experiment demonstrates the feasibility of implementing a QW with a trapped ion. Although the number of steps is small in our experiment, the trapped-ion system clearly reveals its strengths in the high fidelity of the results. The severe limitation on the number of steps for the implementation of the shift operator via the optical dipole force is due to the Lamb–Dicke parameter η , since shifts in terms of the displacement operator are only possible within the LDR (Figures 5 and 6). Our comparatively large Lamb–Dicke parameter $\eta = 0.31$ allows for three well distinguishable ($|\Delta\alpha| = 1$) steps. For a Lamb–Dicke parameter of $\eta = 0.1$ the limit of the LDR is $g_1 = 85$ with a corresponding maximal position state $|\alpha_{max} \approx 9\rangle$ within the LDR. This would allow for a QW with 9 steps of similar fidelity, using our scheme. Equivalently, a Lamb–Dicke parameter of $\eta = 0.06$ would allow for 15 steps. Additionally, since in such a setup the step size is very small compared to the size of the LDR, the threshold g_1 may be

less of a limitation, as it can be overcome via small steps (Cf. figure 8). A QW with up to 23 steps, implemented with a dipole force on resonance ($\delta = 0$), has recently been demonstrated [32]. As described in section 2, a QW with effectively orthogonal position states requires a step size of $|\Delta\alpha| \geq 2$. This reduces the number of steps within the LDR for any given setup. Extending the number of possible steps substantially by further reducing the Lamb–Dicke factor is a difficult task. The trap frequency ω_z has to be increased and the mutual angles of the laser beams providing the dipole force must be reduced (Cf. figure 3b). However, a small Lamb–Dicke factor η yields a weak coupling of the light field to the motional degree of freedom. This weak coupling must be compensated by an increased intensity of the laser beams. This in turn results in an increased rate of spontaneous emission [43] from the off-resonantly excited $|^2P_{3/2}, F = 4\rangle$ states (Figure 4) and thus in a reduced coherence time for the QW.

6. Outlook

6.1. Implementation on the shift operator using photon kicks

In the following we propose the implementation of the shift operator with photon kicks [36, 37], which is substantially less dependent on the motional state and allows for the implementation of QWs with many steps. The principle of a photon kick is to apply a π -pulse on the coin states which is sufficiently short such that the free harmonic motion of the ion during the pulse itself is negligible. It has been shown that the change of the momentum of the ion during such a pulse can be described by a displacement operator, allowing us to propose its application as a building block for the shift operator of a QW. In the original protocol [36], which has been realized recently [49], however, the influence of the motional state on the performance of the photon kicks has not been considered, since the amplitudes of the motional states were assumed to remain small. For the implementation of a QW with many steps, we have to consider (coherent) motional states with very large amplitude and, thus, have to re-assess the validity of the above-mentioned approximation. We find that, for a given fidelity, the upper bound for the pulse duration scales inversely with the motional amplitude, and additionally, for coherent motional states, depends on the phase of their harmonic oscillation at the moment when the pulse is applied. In the following we derive an analytic bound for general states and present the results of a numerical study for coherent motional states. With the latter we show that QWs with up to 100 steps for a step size of $|\Delta\alpha| = 2$ should be possible with state-of-the-art technology.

Referring to [36], we start our analysis with the Hamiltonian

$$\begin{aligned} \mathcal{H} &= \mathcal{H}_0 + \mathcal{H}_1 \\ &= \frac{\Omega}{2} \left(\sigma_+ \otimes e^{i\eta(a^\dagger+a)} + \sigma_- \otimes e^{-i\eta(a^\dagger+a)} \right) + \omega_z a^\dagger a. \end{aligned} \tag{27}$$

This Hamiltonian can be implemented in various ways, e.g. via direct dipole coupling, two-photon stimulated Raman transitions or stimulated Raman adiabatic

passage [36]. Each implementation imposes different constraints on pulse duration, laser intensities, etc. In the following we will focus on the implementation with a two-photon stimulated Raman transition and consider the energy levels of $^{25}\text{Mg}^+$.

In this configuration, two laser beams (R_a, R_b) resonantly drive two-photon transitions between the coin states via a virtual state detuned from the $P_{3/2}$ manifold by Δ_R . Each laser beam drives only one of the two Raman branches, due to their different polarizations. In a RWA, terms varying at optical frequencies are neglected. This is valid in our case for pulse durations well above $1/10^{-15} \text{ Hz} = 1 \text{ fs}$. Finally, an adiabatic elimination of the $P_{3/2}$ states requires $|\Omega/\Delta_R| \ll 1$. The pulse duration T_p in our case must therefore be sufficiently longer than 5 ps for $\Delta_R \approx 2\pi \cdot 10^{11} \text{ Hz}$ and $T_p\Omega = \pi$ (see below). The effective wave vector of the two-photon transition is $\mathbf{k} = \mathbf{k}_a - \mathbf{k}_b$.

Hamiltonian (27) implements the desired displacement operator for a pulse duration of $T_p = \pi/\Omega$, if we neglect the perturbation \mathcal{H}_1 . The time evolution operator then reads

$$\begin{aligned}
 U_0(T_p) &= e^{-i\mathcal{H}_0 T_p} \\
 &= \cos\left(\frac{\Omega T_p}{2}\right) \cdot \mathbb{I}_{\text{coin}} \otimes \mathbb{I}_{\text{motion}} \\
 &\quad - i \sin\left(\frac{\Omega T_p}{2}\right) \cdot (\sigma_+ \otimes D(i\eta) + \sigma_- \otimes D(-i\eta)) \\
 &= -i(\sigma_+ \otimes D(i\eta) + \sigma_- \otimes D(-i\eta)),
 \end{aligned} \tag{28}$$

which is obtained by expanding the exponential function, splitting the series into odd and even parts and using the properties of the Pauli matrices and displacement operators.

The shift operator itself, implementing the desired step size (i.e. $|\Delta\alpha| = 2$, see figure 2), can be realized by the subsequent application of $2/\eta$ kicks in such a way that the displacements $D(i\eta)$ of several π -pulses add up to $D(\Delta\alpha = i\eta \cdot 2/\eta)$. This can be achieved by changing the direction of the effective wave vector by 180° for each photon kick. In practice one can either switch between two Raman beam configurations with opposite effective wave vectors, or implement every second π -pulse by a RF transition for which the momentum transfer is negligible. Notably, with this protocol the step sizes for both directions of the QW are equal, in contrast to the method of optical dipole forces used in our current experiment.

In the following we derive a conservative estimate for the deviation from a coherent-state displacement induced by \mathcal{H}_1 . The total time evolution is

$$U(t) = e^{-i\mathcal{H}t} = U_0(t) \cdot V(t) \tag{29}$$

with $V(t) = e^{i\mathcal{H}_0 t} e^{-i\mathcal{H}t}$. $V(t)$ can be differentiated

$$\dot{V}(t) = -ie^{i\mathcal{H}_0 t} \mathcal{H}_1 e^{-i\mathcal{H}_0 t} \cdot V(t), \tag{30}$$

leading to an equation which is formally solved by the integral equation

$$V(t) = \mathbb{I} - i \int_0^t ds e^{i\mathcal{H}_0 s} \mathcal{H}_1 e^{-i\mathcal{H}_0 s} \cdot V(s), \tag{31}$$

using $V(0) = \mathbf{1}$. Now we define ϵ as the distance between the evolved state according to the full Hamiltonian and the desired evolved state according to \mathcal{H}_0 :

$$\begin{aligned}\epsilon &\equiv \| (U(t) - U_0(t)) |\psi\rangle \| \\ &= \| (V(t) - \mathbf{1}) |\psi\rangle \| \\ &= \left\| \int_0^t ds e^{i\mathcal{H}_0 s} \mathcal{H}_1 e^{-i\mathcal{H}_0 s} V(s) |\psi\rangle \right\|.\end{aligned}\tag{32}$$

Approximating the last expression by the largest term of the first order Dyson series, and considering a motional state $|\psi\rangle = |H\rangle |\alpha\rangle$, gives the following error estimate for a pulse with duration T_p [50]

$$\epsilon \approx \left\| \int_0^{T_p} ds \omega_z \mathbf{1} \otimes a^\dagger a |\psi\rangle \right\| = T_p \omega_z |\alpha|^2.\tag{33}$$

Thus, for an initial state $|H\rangle |\alpha\rangle$ (the coin state can be chosen arbitrarily), the pulse duration T_p necessary to implement the displacement operator with an error smaller than ϵ must fulfill

$$T_p \leq \frac{\epsilon}{\omega_z \cdot |\alpha|^2}.\tag{34}$$

The scaling with $|\alpha|^{-2}$ is, however, a rather rough estimate. This is shown by a numerical simulation of this process, in particular considering the application of photon kicks to (superpositions of) coherent motional states. We compute the fidelity $f = |\langle H | \langle \alpha | U_0^\dagger(T_p) U(T_p) | H \rangle |\alpha\rangle|^2$ with the initial state $|H\rangle |\alpha\rangle$, a pulse duration T_p , and $\Omega = \pi/T_p$, where the time evolution is implemented using a Runge–Kutta method. The results show that the fidelity strongly depends on the phase of ion oscillation at the moment of the photon kick.

Demanding a fidelity of $f \geq 0.99$ and for imaginary α , i.e. at the moment of the photon kick the ion is in the center of the harmonic potential and thus fastest, for our experimental parameters we find §

$$T_{f=0.99}^{\Im}(|\alpha|) = \exp(-17.55 - 0.63 \ln(|\alpha|) - 0.05 (\ln(|\alpha|))^2).\tag{35}$$

For $|\alpha| = 200$, an amplitude reached after the 100th step of a QW with $|\Delta\alpha| = 2$, the pulse duration must be shorter than $T_{f=0.99}^{\Im}(200) = 0.21$ ns.

However, applying the photon kick when the ion is at its turning point, i.e. the ion is slowest and α is real, the scaling is less demanding. We find

$$T_{f=0.99}^{\Re}(|\alpha|) = \exp(-17.03 - 0.02 \ln(|\alpha|) - 0.1 (\ln(|\alpha|))^2).\tag{36}$$

Most importantly, the prefactor of the term linear in $\ln(|\alpha|)$ is much smaller than for an imaginary α . For the 100th step, the pulse duration therefore only has to be shorter

§ Equations (35) and (36) are the results of quadratic fits to double-logarithmic plots of pairs $(T_p, |\alpha|)$ for a fidelity $f = 0.99$ and $|\alpha| \leq 10$. Higher motional amplitudes were not considered due to sizable additional numerical effort. For the following estimates, the scaling is considered to be preserved.

than $T_{f=0.99}^{\mathfrak{R}}(200) = 2.18$ ns, which is within the specifications of a fast-switching electro-optic modulator and our current continuous-wave laser system. Timing the application of the photon kick to the (spatial) turning points of all the coherent oscillations occurring during the QW is possible, because we start the QW in the motional ground state and the position states are aligned along a line in the co-rotating phase space. Thus, coherent states of different $|\Delta\alpha|$ reach their turning points simultaneously.

Given our experimental parameters, in particular the width of the ground state wave function $z_0 = 10$ nm, the coherent motional state of maximal amplitude, $|\alpha_{max} = 200\rangle$, would have a real-space amplitude of $\langle\alpha_{max}|z|\alpha_{max}\rangle = 4$ μm . At such high motional amplitudes anharmonicities of the trapping potential must be considered. These depend on the design of the electrodes and could be eliminated, e.g. by designing the Paul trap electrodes in a hyperbolic shape [51]. Additionally, micromotion might increase the deviation from the ideal walk, for example by reducing the overlap of the additionally oscillating motional wave functions. However, it will remain negligible when the QW is implemented in the axial degree of freedom of an ion in a linear Paul trap.

6.2. QW in higher dimensions

A QW in two or three dimensions is possible by additionally considering the motion in the radial direction. The pulse sequence for a step of a QW is then the subsequent application of the shift operator in each direction where each operation is preceded by a coin toss.

More possibilities and reduced technical requirements might be achieved by trapping more than one ion and considering the collective degrees of motion in one direction. Reference [52] describes the scheme with two ions, creating a 4-sided coin, where two coin states affect the walk in the center-of-mass motional mode and the other two in the stretch mode of motion. In particular, possibilities with the coin being initialized in an entangled state are investigated.

A photon kick, as described above, induces motion in all motional modes in the direction of the effective wave vector \mathbf{k} , according to the respective coin states. That is, with N ions, one step of the QW consists of a coin operation on the 2^N -sided coin and a single shift operation, that displaces the part of the motional wave function related to each coin state into opposite direction in phase space of one motional mode. The particular difficulty is to assign the 2^{N-1} pairs of coin states to N different axial motional modes such that for each coin state the corresponding state dependent force induces motion in one direction in one certain mode [53]. One possibility to obtain the required number of motional modes is to add ions that do not contain a transition corresponding to the coin states and therefore are not affected by the photon kicks. That would be in our case ^{24}Mg ions without hyperfine structure and therefore no coin states and no corresponding transition. With this, the implementation of a QW in four dimensions is possible using three ^{25}Mg ions and one ^{24}Mg ion. For more dimensions the issue arises that the ^{24}Mg and ^{25}Mg ions have to be arranged in such a way that for

each coin state the corresponding state dependent force induces motion in one certain mode, which has not been clarified yet.

Acknowledgements

This work was supported by MPQ, MPG, DFG (SCHA 973/1-6), the EU via SCALA and STReP PICC, and the DFG Cluster of Excellence “Munich-Centre for Advanced Photonics”. RM acknowledges support by the EU project COQUIT. We thank J. J. García-Ripoll for intriguing discussions about the short-pulse scheme, M. J. McDonnell for assistance with the simulation code, and Ignacio Cirac, Gerhard Rempe and Reinhard Werner for their great intellectual and financial support.

References

- [1] Barber M N and Ninham B W 1970 *Random and restricted walks: theory and applications* (New York: Gordon and Breach)
- [2] Berg H C 1993 *Random walks in biology* (Princeton, NJ: Princeton University Press)
- [3] Aharonov Y, Davidovich L and Zagury N 1993 *Phys. Rev. A* **48** 1687–1690
- [4] Kempe J 2003 *Contemp. Phys.* **44** 307–327
- [5] Grover L K 2001 *Am. J. Phys.* **69** 769–777
- [6] Gross D, Nesme V, Vogts H and Werner R F 2009 *arxiv:quant-ph/0910.3675*
- [7] Childs A M 2009 *Phys. Rev. Lett.* **102** 180501
- [8] Ambainis A 2007 *SIAM J. Comput.* **37** 210–239
- [9] Shenvi N, Kempe J and Whaley K B 2003 *Phys. Rev. A* **67** 052307
- [10] Shikano Y, Chisaki K, Segawa E and Konno N 2010 *Phys. Rev. A* **81** 062129
- [11] Engel G S, Calhoun T R, Read E L, Ahn T K, Mančal T, Cheng Y C, Blankenship R E and Fleming G R 2007 *Nature* **446** 782–786
- [12] Mohseni M, Rebentrost P, Lloyd S and Aspuru-Guzik A 2008 *J. Chem. Phys.* **129** 174106
- [13] Ahlbrecht A, Alberti A, Meschede D, Scholz V B, Werner A H and Werner R F 2011 *arXiv:quant-ph/1105.1051*
- [14] Ahlbrecht A, Scholz V B and Werner A H 2011 *arXiv:quant-ph/1101.2298*
- [15] Ahlbrecht A, Vogts H, Werner A H and Werner R F 2011 *J. Math. Phys.* **52** 042201
- [16] Chandrashekar C M, Banerjee S and Srikanth R 2010 *Phys. Rev. A* **81** 062340
- [17] Ryan C A, Laforest M, Boileau J C and Laflamme R 2005 *Phys. Rev. A* **72** 062317
- [18] Mandel O, Greiner M, Widera A, Rom T, Hänsch T W and Bloch I 2003 *Phys. Rev. Lett.* **91** 010407
- [19] Dür W, Raussendorf R, Kendon V M and Briegel H J 2002 *Phys. Rev. A* **66** 052319
- [20] Karski M, Förster L, Choi J M, Steffen A, Alt W, Meschede D and Widera A 2009 *Science* **325** 174–177
- [21] Eckert K, Mompert J, Birkl G and Lewenstein M 2005 *Phys. Rev. A* **72** 012327
- [22] Chandrashekar C M 2006 *Phys. Rev. A* **74** 032307
- [23] Bouwmeester D, Marzoli I, Karman G P, Schleich W and Woerdman J P 1999 *Phys. Rev. A* **61** 013410
- [24] Schreiber A, Cassemiro K N, Potoček V, Gábris A, Mosley P J, Andersson E, Jex I and Silberhorn C 2010 *Phys. Rev. Lett.* **104** 050502
- [25] Perets H B, Lahini Y, Pozzi F, Sorel M, Morandotti R and Silberberg Y 2008 *Phys. Rev. Lett.* **100** 170506
- [26] Peruzzo A, Lobino M, Matthews J C F, Matsuda N, Politi A, Poullos K, Zhou X Q, Lahini Y,

- Ismail N, Wörhoff K, Bromberg Y, Silberberg Y, Thompson M G and OBrien J L 2010 *Science* **329** 1500–1503
- [27] Schaetz T, Schneider C, Enderlein M, Huber T and Matjeschk R 2011 *ChemPhysChem* **12** 71–74
- [28] Travaglione B C and Milburn G J 2002 *Phys. Rev. A* **65** 032310
- [29] Wineland D and Leibfried D 2011 *Laser Phys. Lett.* **8** 175–188
- [30] Schmitz H, Matjeschk R, Schneider C, Glueckert J, Enderlein M, Huber T and Schaetz T 2009 *Phys. Rev. Lett.* **103** 090504
- [31] Xue P, Sanders B C and Leibfried D 2009 *Phys. Rev. Lett.* **103** 183602
- [32] Zähringer F, Kirchmair G, Gerritsma R, Solano E, Blatt R and Roos C F 2010 *Phys. Rev. Lett.* **104** 100503
- [33] McDonnell M J, Home J P, Lucas D M, Imreh G, Keitch B C, Szwer D J, Thomas N, Webster S C, Stacey D N and Steane A M 2007 *Phys. Rev. Lett.* **98** 063603
- [34] Poschinger U, Walther A, Singer K and Schmidt-Kaler F 2010 *Phys. Rev. Lett.* **105** 263602
- [35] Schmitz H, Friedenauer A, Schneider C, Matjeschk R, Enderlein M, Huber T, Glueckert J, Porras D and Schaetz T 2009 *Appl. Phys. B* **95** 195–203
- [36] García-Ripoll J J, Zoller P and Cirac J I 2003 *Phys. Rev. Lett.* **91** 157901
- [37] García-Ripoll J J, Zoller P and Cirac J I 2005 *Phys. Rev. A* **71** 062309
- [38] Schaetz T, Friedenauer A, Schmitz H, Petersen L and Kahra S 2007 *J. Mod. Opt.* **54** 2317–2325
- [39] Wineland D J, Monroe C, Itano W M, Leibfried D, King B E and Meekhof D M 1998 *J. Res. Natl. Inst. Stand. Technol.* **103** 259–328
- [40] Leibfried D, Blatt R, Monroe C and Wineland D 2003 *Rev. Mod. Phys.* **75** 281–324
- [41] Monroe C, Meekhof D M, King B E, Jefferts S R, Itano W M, Wineland D J and Gould P 1995 *Phys. Rev. Lett.* **75** 4011–4014
- [42] Wineland D J and Itano W M 1979 *Phys. Rev. A* **20** 1521–1540
- [43] Wineland D J, Barrett M, Britton J, Chiaverini J, DeMarco B, Itano W M, Jelenković B, Langer C, Leibfried D, Meyer V, Rosenband T and Schätz T 2003 *Phil. Trans. R. Soc. Lond. A* **361** 1349–1361
- [44] Leibfried D, DeMarco B, Meyer V, Lucas D, Barrett M, Britton J, Itano W M, Jelenković B, Langer C, Rosenband T and Wineland D J 2003 *Nature* **422** 412–415
- [45] Monroe C, Meekhof D M, King B E and Wineland D J 1996 *Science* **272** 1131–1136
- [46] Wallentowitz S and Vogel W 1997 *Phys. Rev. A* **55** 4438–4442
- [47] Carruthers P and Nieto M M 1965 *Am. J. Phys.* **33** 537–544
- [48] Meekhof D M, Monroe C, King B E, Itano W M and Wineland D J 1996 *Phys. Rev. Lett.* **76** 1796–1799
- [49] Campbell W C, Mizrahi J, Qurashi Q, Senko C, Hayes D, Hucul D, Matsukevich D N, Maunz P and Monroe C 2010 *Phys. Rev. Lett.* **105** 090502
- [50] García-Ripoll J J priv. comm.
- [51] Paul W 1990 *Rev. Mod. Phys.* **62** 531–540
- [52] Omar Y, Paunković N, Sheridan L and Bose S 2006 *Phys. Rev. A* **74** 042304
- [53] James D F V 1998 *Appl. Phys. B* **66** 181–190